A NUMERICAL INVESTIGATION OF THE BACK REACTION OF DUST AND GAS ON ACCRETION DISC MORPHOLOGY

by

MATTHEW MURRAY

(Under the Direction of Cassandra Hall)

ABSTRACT

The mass of a protoplanetary disc is exceptionally difficult to observe directly due to the dimness of molecular hydrogen and the optical thickness of the gas portion of a typical accretion disc. A common method for determining mass constraints in PPDs is to use the flux of continuum observations to approximate the mass of the optically thin dusty midplane, and then use an assumed ϵ mass ratio to constrain total mass. This work shows the importance of considering effects from dust on disc morphology, namely depth of gaps induced by planets. I show that for fixed dust mass and a constant grain size, gap depths decrease for increasing ϵ. Since the dust mass of a disc can be inferred through continuum observations, the depth of a gap in dust can be used to additionally constrain the ϵ mass ratio. For multiple discs with planets of similar mass, we can rank the discs by their ϵ mass ratios based on measured gap depth. Additionally, I propose an update to the current analytical gap depth prescription that includes effects due to the back reaction and variations in ϵ mass ratio.

INDEX WORDS: [Smooth Particle Hydrodynamics, Accretion Disc, Protoplanetary Disc, Numerical Analysis, Dust-to-Gas Ratio]

A Numerical Investigation of the Back Reaction of Dust and Gas on Accretion Disc Morphology

by

Matthew Murray

B.A., University of Colorado: Boulder, 2019

A Thesis Submitted to the Graduate Faculty of the
University of Georgia in Partial Fulfillment of the Requirements for the
Degree.

Master of Science

Athens, Georgia

2024

A Numerical Investigation of the Back Reaction of Dust and Gas on Accretion Disc Morphology

by

Matthew Murray

Major Professor:	Cassandra Hall
Committee:	Inseok Song Phillip C. Stancil

Electronic Version Approved:

Ron Walcott
Dean of the Graduate School
The University of Georgia
August 2024

DEDICATION

To all of the scientists who have come before me, patient teachers who have made this possible, and anyone who has looked to the night sky with wonder.

To my parents, the first scientists in my life, both literally and first in my regard, who nurtured my curiosity and tolerated a kid who's mouth ran faster than his sense.

To my beloved teachers, Mrs. Morris, Mrs. Turegano, and Dr. David Brain for your patience, knowledge, and infectious excitement setting me on this path when I was eighteen.

To my colleagues and friends who provided so much encouragement and love at every step.

To my ancestors from time immemorial who first looked up to the sky and told stories; yours is a tradition I am proud to carry.

"If I have seen further [than others], it is by standing on the shoulders of giants."
- Letter from Sir Isaac Newton to Robert Hooke, 1675

ll

ACKNOWLEDGMENTS

I would like to thank the Physics and Astronomy faculty: Dr. Cassandra Hall for her support and enthusiasm as my research advisor, Dr. Philip Stancil and Dr. Inseok Song for serving on my committee, and Dr. Nandana Weliweriya for being an inspiration in the classroom.

I would like to thank the members of my research group: Hans Baehr, Jason Terry, James "Jimmy" Sarget, and Ian Drury for valuable insights at our weekly research meetings and their time helping to proofread.

Final thanks to Dr. Daniel Price of Monash University, whom I have never met, but who's work on `PHANTOM` has made all of this possible.

And to my parents, Kermit Murray and Michelle Beeson, for their unwavering support, encouragement, and the occasional kick in the rear when I needed it.

CONTENTS

CHAPTER 1

INTRODUCTION AND LITERATURE REVIEW

There are now over 5000 confirmed exoplanets, revealing huge diversity in the exoplanet architecture. Arguably the most fundamental exoplanet properties are semi-major axis and planetary mass, which vary by over three to four orders of magnitude in the known population (Zhu and Dong, 2021). A planet's semi-major axis may be heavily influenced by planet-disc interactions that lead to migration early in the disc's life (Kley and Nelson, 2012), but may also continue to evolve under secular interactions well after disc dispersal (Ida et al., 2000). Obtaining an accurate measurement of protoplanetary disc (PPD) mass is crucial to understanding the diversity of exoplanets, because planetary masses are constrained by the overall mass budget in a PPD.

Disc mass is also one of the most challenging characteristics to constrain through observations. The molecule with the largest share by mass of any PPD, molecular hydrogen, emits very weakly at typical disc temperatures (Carmona, 2010). As a result, total mass estimates are challenging to obtain directly, and as such are typically inferred indirectly.

One of the most common methods of determining PPD mass involves using a tracer molecule such as CO, which is about 10 million times more emissive than H_2 at typical disc temperatures (Bergin and Williams, 2017). However, this is not without complications. The lines of some CO isotopologues may be optically thick, therefore only tracing the upper layers of the disc and masking emission from deeper layers which gives an incomplete account of the total emission from that tracer. Additionally, there are uncertainties in the assumed abundances which may be affected and altered by chemical reactions and photodissociation. An alternative that has emerged recently is the measurement or constraint of disc mass through dynamical or kinematic means (Longarini et al., 2021; Pinte et al., 2023; Terry et al., 2022; Veronesi et al., 2021), although this requires that the disc be sufficiently massive to be self-gravitating.

The method we are the most interested in uses the brightness of continuum emissions to obtain the total dust mass (Andrews et al., 2012), and then infers both the gas and total mass based on an assumed dust-to-gas mass ratio, ϵ. Measuring the total dust emission is less challenging since it emits over a continuum, but there are still significant sources of uncertainty. For example the dust opacity can vary widely depending on a number of assumed properties such as temperature, composition, size, and porocity, such that the dust emission can be either optically thin or thick at millimeter wavelengths based on the choice of dust opacity (Xin et al., 2023). Particles of larger sizes (typically $\sim$mm and above) undergo differential settling and radial drift, resulting in size segregation of grains across the disc (Youdin and Lithwick, 2007).

Perhaps the strongest source of uncertainty is the assumed ϵ. Best estimates for ϵ in the interstellar medium (ISM) are $\epsilon \sim 0.01$(Frisch and Slavin, 2003; Frisch et al., 2011; Nguyen et al., 2018), and as a result this is a commonly assumed value for PPDs. However, this is likely an oversimplification. For example, observations of CO have found that the average disc ϵ values can be substantially higher, reaching around 0.2 (Ansdell et al., 2016). Similarly, simulations, such as those by Lebreuilly et al., 2020, have shown that discs can form with significant dust enrichment. Compounding this is the large discrepancy between the observed radial extent of the gas and dust disc components, with the latter typically appearing far more compact (Andrews et al., 2012; Pérez et al., 2012, 2015) due to a combination of grain growth and radial drift. In the most extreme cases the dust disc can be 10 times more compact than its gas component (see observations of IM Lup (Cleeves et al., 2016)), and since $\epsilon = \epsilon_{\rm ISM}[R_{\rm gas\,disc}/R_{\rm dust\,disc}]^2$ (Ilee et al., 2020), this could potentially result in ϵ values as high as $\epsilon = 1.0$ in the inner $\sim$ 120 au of the disc.

Observations with the Atacama Large Millimeter/submillimeter Array (ALMA) over the last decade have identified a plethora of previously unobserved substructure within PPDs, in particular rings and gaps in the dust continuum (ALMA Partnership et al., 2015; Andrews et al., 2018), spirals (Huang et al., 2018), and velocity perturbations in CO line emission (Pinte et al., 2018; Teague et al., 2018). Velocity perturbations are a strong indication of the kinematic influence of protoplanets (Pinte et al., 2020), which may lead to the formation of these observed disc structures. The observed morphology of this ring-like structure is a function of both planet and disc properties, and can be used to constraint these properties.

In this work, we demonstrate how changing global ϵ ratios affects the morphology of PPDs with an embedded planet. Understanding the causality can be used to qualitatively constrain the ϵ values in observed systems, and can be effective in systems where protoplanet mass is constrained by kinematics. Additionally we show ways in which the current prescription for predicting and analyzing gap depths deviates from simulated results when considering effects of the back reaction. We do this by simulating PPDs with embedded planets using smoothed particle hydrodynamics (SPH) across a variety of disc masses, ϵ, and dust-gas coupling ratios to isolate the effects ϵ has on a disc's morphology.

This thesis is organized as follows: The first chapter will serve as an introduction and literature review, discussing accretion discs and dusty PPDs, smoothed particle hydrodynamics, planet-disc interactions, and the specific parameters of simulations performed. The second chapter is a presentation of my contribution as a manuscript submitted to The Monthly Notices of the Royal Astronomical Society. The third and final chapter situates my results in the context of the field, with a short discussion of potential future work.

1.1 Protoplanetary Discs: Model, Evolution, and Observations

Models and dynamics of PPDs extend from early work on accretion discs around black holes and X-ray emitting stars (Pringle, 1981). PPDs can be thought of as a specific case of accretion discs, as both form from large clouds of viscous gas in potential wells (Jefferys, 1924; von Weizsäcker, 1948). Typically these potential wells are gravitational potentials about stars or black holes. Viscous interaction, kinetic energy exchange through collisions, and conservation of angular momentum causes the gas to settle into a relatively thin disc with significantly more radial extent than vertical (Nakagawa et al., 1986). As a parcel of gas falls towards the central star, vertically or radially into the gravitational well, it speeds up (Hoyle, 1960; marquis de Laplace, 1813). Viscous interactions impart a portion of that velocity onto the slower moving gas parcels further from the central mass, speeding them up and sending them outward, conserving angular momentum (Papaloizou and Lin, 1995). If you imagine a cloud with initial radius $r = R_0$ that collapses into a torus of approximately the same radius, the majority of the mass comprising the ring is sent to $r < R_0$, with exterior gas dispersing further and further ($r > R_0$) from the central star.

The specific origin of viscous interaction is disputed and uncertain, but mathematical models have had great success parameterizing it via the overall efficiency of angular momentum transport. The landmark "α-prescription" described in Shakura and Sunyaev, 1973 is used to characterize accretion discs to this day. This is a very effective mathematical model, but was developed post-hoc to resolve divergence between previous mathematical models and observations. The modern solution is to use numerical simulation of accretion discs, treating the gas and suspended dust as viscous fluids with the Navier-Stokes equations, and then compare the results to observations (Dipierro, Price, et al., 2015a; Speith et al., 1999; Stone, 1994).

1.1.1 Navier-Stokes and Gas Dynamics

The Navier-Stokes[1] equations are partial differential equations that describe the movement of viscous fluids. The N-S Equations are much studied in fluid dynamics, but no closed form, generalized solution yet exists (Ladyzhenskaya, 2003). Never-the-less there are useful analytical solutions for specific applications. The most general form is as follows[2]:

$$\frac{\partial \rho}{\partial t} + \nabla \cdot (\rho \boldsymbol{v}) = 0 \tag{1.1}$$

$$\frac{\partial}{\partial t}(\rho \boldsymbol{v}) + \nabla \cdot (\rho \boldsymbol{v} \otimes \boldsymbol{v}) = -\nabla p + \nabla \cdot \boldsymbol{\tau} + \rho \boldsymbol{g} \tag{1.2}$$

Where, ρ is the density of the fluid, $\boldsymbol{v}$ is the velocity field that describes fluid motion, p is pressure, $\boldsymbol{\tau}$ is a stress tensor, and $\boldsymbol{g}$ is any body force or acceleration. In most astrophysical applications, this commonly includes gravitational potentials and can include other potentials, for example the effects of magnetism. Equation 1.1 is a constraint on continuity, and Equation 1.2 is the general form for an equation of motion of a fluid. For component wise derivations of the velocities of dust and gas, we follow Dipierro and Laibe, 2017 for it's explicit presentation of steady state solutions to the N-S equations.

To begin solving, a substitution of quantities describing gas and dust is all that is needed to bring Equation 1.2 into the use case of PPDs:

$$\frac{\partial \boldsymbol{v}_{\mathrm{g}}}{\partial t} + (\boldsymbol{v}_{\mathrm{g}} \cdot \nabla)\boldsymbol{v}_{\mathrm{g}} = \frac{K}{\rho_{\mathrm{g}}}(\boldsymbol{v}_{\mathrm{d}} - \boldsymbol{v}_{\mathrm{g}}) - \nabla(\Phi + \Phi_{\mathrm{p}}) - \frac{1}{\rho_{\mathrm{g}}}(\nabla P - \nabla \cdot \sigma) \tag{1.3}$$

$$\frac{\partial \boldsymbol{v}_{\mathrm{d}}}{\partial t} + (\boldsymbol{v}_{\mathrm{d}} \cdot \nabla)\boldsymbol{v}_{\mathrm{d}} = \frac{K}{\rho_{\mathrm{d}}}(\boldsymbol{v}_{\mathrm{d}} - \boldsymbol{v}_{\mathrm{g}}) - \nabla(\Phi + \Phi_{\mathrm{p}}) \tag{1.4}$$

The "g" and "d" subscripts refer to the gas and dust phases respectively, Φ and Φ_p are gravitational potentials due to the star and planet respectively, and K is a term quantifying the coupling of dust and gas related to the stopping time, t_{s}, and dust-to-gas ratio, ϵ. Note that both phases are treated under the same

[1] Hereafter "N-S"

[2] Bold symbols (e.g. $\boldsymbol{v}$) indicate vector quantities.

prescription, save for pressure (P) and viscosity (σ) present in the gas phase. This is because only gas is pressure supported and viscous. Dust feels neither of these directly, instead the drag coupling K is how viscosity and pressure information are communicated to the dust (Laibe and Price, 2012):

$$K \equiv \frac{\rho_{\mathrm{d}}}{t_{\mathrm{s}}(1+\epsilon)}. \tag{1.5}$$

Related t_{s} is the Stokes number, St:

$$t_{\mathrm{s}} = \frac{\mathrm{St}}{\Omega_{\mathrm{k}}}. \tag{1.6}$$

The Stokes number is related to drag and is a direct way of parameterizing of the degree of coupling felt between a fluid and some solid particle(s) it hosts. Ω_{k} is the Keplerian Orbital Period about a host star of mass M_* at a radius r, is given by

$$\Omega_{\mathrm{k}} = \sqrt{\frac{GM_*}{r^3}}, \tag{1.7}$$

And serves as the fiducial orbital period for a completely uncoupled dust grain ($\mathrm{St} \approx +\infty$) or a pressureless gas. In a PPD, dust particles with high Stokes numbers ($\mathrm{St} >> 1$) are uncoupled from the host gas and move without influence from the gas; think like a rock in a river bed. Dust particles with low Stokes numbers ($\mathrm{ST} << 1$) are coupled to the host gas and are strongly influenced by it; think like a leaf floating in a river. To find the Stokes number of a given grain species in a fluid, we follow Birnstiel et al., 2010:

$$\mathrm{St} = \frac{\pi a \rho_{\mathrm{s}}}{2\Sigma_{\mathrm{g}}}, \tag{1.8}$$

Where ρ_{s} is the bulk density of the dust species being considered, typically taken to be $\approx 3\mathrm{g} \cdot \mathrm{cm}^{-3}$. Σ_{g} is the gas surface density. Note that by rearranging Equation 1.6, one can also express the stokes number as the product of the stopping time and orbital period:

$$\mathrm{St} = t_{\mathrm{s}}\Omega_{\mathrm{k}} \tag{1.9}$$

To solve for the non-ideal case of pressure supported gas with dust of arbitrary coupling, perform a perturbative expansion around the Keplerian velocity, $\boldsymbol{v}_{\mathrm{k}} = (0, r\Omega_{\mathrm{k}}, 0)$. We continue following Dipierro and Laibe, 2017.

Do this in both gas and dust phases to a acquire a system of differential equations describing $\frac{\partial v_{\mathrm{g,R}}}{\partial t}$, $\frac{\partial v_{\mathrm{g,\Phi}}}{\partial t}$, $\frac{\partial v_{\mathrm{d,R}}}{\partial t}$, and $\frac{\partial v_{\mathrm{d,\Phi}}}{\partial t}$:

$$\frac{\partial v_{\rm g,R}}{\partial t} = \frac{K}{\rho_{\rm g}}(v_{\rm d,r} - v_{\rm g,r}) - \frac{1}{\rho_{\rm g}}\frac{\partial P}{\partial r} + 2\Omega_{\rm k} v_{\rm g,\theta}, \tag{1.10}$$

$$\frac{\partial v_{\rm g,\phi}}{\partial t} = \frac{K}{\rho_{\rm g}}(v_{\rm d,\theta} - v_{\rm g,\theta}) - \frac{\Omega_{\rm k}}{2} v_{\rm g,2} + \frac{1}{\rho_{\rm g}}\nabla\cdot\sigma|_\theta + \frac{\Lambda_{\rm g}}{r}, \tag{1.11}$$

$$\frac{\partial v_{\rm d,R}}{\partial t} = \frac{K}{\rho_{\rm g}}(v_{\rm d,r} - v_{\rm g,r}) + 2\Omega_{\rm k} v_{\rm d,\theta}, \tag{1.12}$$

and

$$\frac{\partial v_{\rm d,\phi}}{\partial t} = \frac{K}{\rho_{\rm g}}(v_{\rm d,\theta} - v_{\rm g,\theta}) - \frac{\Omega_{\rm k}}{2} v_{\rm d,r} + \frac{\Lambda_{\rm d}}{r}. \tag{1.13}$$

Next, find the stationary solutions to this system of differential equations of the form $X'(t) + AX(t) = B$ to find expressions for the radial and azimuthal velocities of dust and gas. For more detail, we direct the reader to Dipierro and Laibe, 2017, as this is beyond the scope of my study. We are immediately interested in the viscously mediated differential azimuthal velocities of dust and gas:

$$v_{\rm d,\theta} - v_{\rm g,\theta} = -\frac{\Delta v}{2(1+{\rm St}^{-2})} - \frac{v_{\rm visc}}{{\rm St}+{\rm St}^{-1}} - \frac{\Lambda_{\rm g} - \Lambda_{\rm d}}{v_{\rm k}(1+\epsilon)({\rm St}+{\rm St}^{-1})} \tag{1.14}$$

In the simplest possible case, gas and dust with no excitation torque ($\Lambda_{\rm g} = \Lambda_{\rm d} = 0$), have their differential velocities mediated by viscous evolution:

$$v_{\rm d,\theta} - v_{\rm g,\theta} = -\frac{\Delta v}{2(1+{\rm St}^{-2})} - \frac{v_{\rm visc}}{2({\rm St}+{\rm St}^{-1})}. \tag{1.15}$$

Δv is the optimal drift velocity derived in Nakagawa et al., 1986 and $v_{\rm visc}$ is the viscous velocity from Lynden-Bell and Pringle, 1974.

As the phases move independently, they exert a gravitational torque on each other. For a given annulus, the relative azimuthal velocity of the gas and the dust imparts a drag torque, $\Lambda_{\rm g\to d}$, from the gas phase to the dust phase given by:

$$\Lambda_{\rm g\to d} = -r \times \frac{K}{\rho_{\rm d}}(v_{\rm d,\theta} - v_{\rm g,\theta}) \tag{1.16}$$

For a set of given azimuthal velocities, the torque deposited into the dust phase by gas is scaled by the drag coupling, K, which is itself a function of $t_{\rm s}$ and ϵ (Equation 1.5).

At the same time, dust exerts a torque back on the gas via mutual drag. This can be thought of a force pair, naively described by Newton's Third Law that demands an equal and opposite reaction. Except, while proportional, it is not exactly equal in magnitude. The so-called "back reaction" scales that response by the mass ratio, ϵ (Dipierro and Laibe, 2017):

$$\Lambda_{\mathrm{d}\to\mathrm{g}} = -\epsilon\Lambda_{\mathrm{g}\to\mathrm{d}}. \tag{1.17}$$

And this is the quantity we are most interested in. By simulating the back reaction and scaling ϵ we are able to alter drag dynamics as the response torque from the dust directly impedes the movement of gas (Dipierro et al., 2018). To the first order, this leads to an overall reduction in the net torque experienced by a parcel of the dust and/or gas:

$$\begin{aligned}\Lambda_{\mathrm{net}} &= \Lambda_{\mathrm{g}\to\mathrm{d}} + \Lambda_{\mathrm{d}\to\mathrm{g}}\\ &= \Lambda_{\mathrm{g}\to\mathrm{d}} - \epsilon\Lambda_{\mathrm{g}\to\mathrm{d}}\\ &= \Lambda_{\mathrm{g}\to\mathrm{d}}(1-\epsilon).\end{aligned} \tag{1.18}$$

The back reaction due to dust is frequently not included in simulations for computational simplicity, leveraging the assumption that for values of ϵ observed in the ISM ($\epsilon \sim 0.01$), the effects are negligible. Previous findings and simulations, such as Dipierro et al., 2018, have demonstrated that for high values of ϵ the back reaction is certainly not negligible. By simulating PPDs with and without the back reaction, we will show that even relatively small values of and variations in ϵ have measurable effects on the morphology of a dusty disc.

1.2 Smoothed Particle Hydrodynamics

We perform three-dimensional hydrodynamical simulations of pressure-supported, viscous, dusty, gaseous protoplanetary discs (PPDs) using `PHANTOM`, a smoothed particle hydrodynamics (SPH) code (Price et al., 2018b). We use the one-fluid approximation, simulating dust and gas as a single fluid (Jacquet et al., 2011; Laibe and Price, 2014a, 2014b, 2014d; Youdin and Goodman, 2005) with enforced dust mass conservation (Ballabio et al., 2018). We use two different dust prescriptions as scenarios we investigate: The first is dust grains of constant size and is treated normally under SPH; the second is dust grains of variable size, but a constant Stokes number enforced throughout the disc.

1.2.1 Basics of SPH

Smoothed particle hydrodynamics is part of a long line of algorithms used to study the solutions to hydrodynamics problems, namely analytically solving the N-S discussed in the previous section (Gingold and Monaghan, 1977). Continuous field problems are in general difficult to solve, but can be especially so as the problems get further from any sort of simplifying symmetry. One method of handling these problems analytically is to discretize the volume occupied, dividing it into cells, and using the N-S equations at the boundaries of each cell to keep track of flow into and out of a given cell.

When simulating hydrodynamics is there is an implicit tension to using volume elements to determine resolution. The simulation setup that optimizes the resolution is incredibly taxing in memory and computation time, since close-to-empty cells still have a computed flux and empty cells still need to remembered to be empty. One solution to this is known as "Adaptive Mesh Refinement" (AMR) as seen in `FARGO` and it's successor `FARGO3D` (Benítez-Llambay and Masset, 2016; F. Masset, 2000). Fluids move in and out of cells who's size are updated regularly and sometimes nested in order to bring the highest resolution to complicated or otherwise interesting areas of the domain (Berger and Colella, 1989). This does result in the spatial domain not being smoothly sampled, introducing error in certain applications such as turbulent flow (Plewa and Müller, 2001). This makes SPH more suitable for my purposes since we are interested in the large-scale spatial domains of simulating an entire PPD.

To briefly and intuitively develop a working understanding of SPH, imagine a simple volume of $V = L^3$ with some amount of a fluid in it, characterized by a total, mass, M_f. We can discretize the fluid with it's density, $\rho_f = M_f \cdot V^{-1}$, by randomly sampling of a number particles corresponding to the desired resolution, using ρ_f as a probability distribution. This creates a group of particles who's behavior is, at this snapshot in time, identical to the behavior of the fluid. Evolving a discrete set of particles under field conditions (namely velocity, pressure, and potentials) is straightforward when given a particular time step. Additionally, converting back to "smooth" density, ρ_s, from a collection of randomly sampled particles can be achieved with a smoothing kernel (Gingold and Monaghan, 1977):

$$\rho_\mathrm{s}(\boldsymbol{r}) = \int W(\boldsymbol{r} - \boldsymbol{r'})\rho(\boldsymbol{r'})d\boldsymbol{r'} \tag{1.19}$$

Where W satisfies:

$$\int W(\boldsymbol{r})d\boldsymbol{r} = 1 \tag{1.20}$$

Importantly, the smoothing kernel, W, is chosen with respect to the problem. In astrophysical applications the kernel is additionally represented as a function of a smoothing length, h, to preserve local rather than global density (Monaghan and Lattanzio, 1985). The particular choices of W and h for `PHANTOM` will be discussed in Section 1.2.2.

If $\rho(\boldsymbol{r}')$ is unknown or prohibitive to find, $\rho_N \approx \rho_{\rm s}$ can still be approximated from N points utilizing a Monte Carlo integral approximation (Hammersley and Handscomb, 1964).

$$\rho_N(\boldsymbol{r}) = \frac{M}{N}\sum_{j=1}^{N} W(\boldsymbol{r} - \boldsymbol{r}_j) \tag{1.21}$$

Where:

$$M = \int \rho(\boldsymbol{r}) d\boldsymbol{r} \tag{1.22}$$

Thus we have the basic algorithm formulation for SPH: a scheme by which physical and astrophysical problems involving fluids can be solved through statistically smoothing a distribution of particles, who's body forces are much easier to calculate. One of the distinct advantages is that computation power is focused in the areas of highest density, due to the kernel: $W(\boldsymbol{r} - \boldsymbol{r}_j)$. With this formulation, the point particles that carry the mass and density distribution information are also what determine the resolution. Each particle carries with it a local mesh with a range of influence set by a smoothing parameter. This ensures areas that contain more particles necessarily have higher resolution due to multiple overlapping local mesh. Now consider an area with much fewer particles, that region of the simulated space has lower resolution and uses less computation power, because fewer particles fall within each other's local meshes.

The Two-Fluid Formalism

In the two-fluid approximation gas and dust of a PPD are handled as explicitly separate, with a gas and a potentially heterogeneous mixture of diffuse dust grains. Dust grains are categorized into homogeneous species, but still treated as a singular SPH "fluid". Treating the gas and the dust separately, there are two mass continuity equations from the N-S formalism:

$$\frac{\partial \hat{\rho}_{\rm g}}{\partial t} + \nabla \cdot (\hat{\rho}_{\rm g}\boldsymbol{v}_{\rm g}) = 0, \tag{1.23}$$

$$\frac{\partial \hat{\rho_{\mathrm{d}}}}{\partial t} + \nabla \cdot (\hat{\rho_{\mathrm{d}}} \boldsymbol{v}_{\mathrm{d}}) = 0. \tag{1.24}$$

Where $\hat{\rho_{\mathrm{g}}}$ and $\hat{\rho_{\mathrm{d}}}$ are the volume densities of gas and dust respectively. Since solid dust grains occupy a finite volume, it is typical to identify the volume density as the "volume occupied per unit total volume" (Harlow and Amsden, 1975):

$$\theta = 1 - \frac{\hat{\rho_{\mathrm{d}}}}{\rho_{\mathrm{d}}}. \tag{1.25}$$

In astrophysical applications, typical values of ρ_{d} mean that $\theta \approx 1$, but is still included here for completeness.

The momentum conservation of the N-S equations are coupled by the explicit drag term: $\boldsymbol{F}^{V}_{\mathrm{drag}}$. Formally, calculation of drag requires averaging a local drag stress tensor over the surface area of dust grains in that unit volume. Fortunately, for dust particles of the same mass, size, and intrinsic density the momentum exchange due to drag simplifies to (Laibe and Price, 2012):

$$\boldsymbol{F}^{V}_{\mathrm{drag}} = \frac{\hat{\rho_{\mathrm{d}}}}{m_{\mathrm{d}}} K_{\mathrm{s}} (\boldsymbol{v}_{\mathbf{g}} - \boldsymbol{v}_{\mathbf{d}}) \tag{1.26}$$

where K_{s} is the same drag coefficient from Equation 1.5.

The primary equations of motion are expressions of the individual momenta of each SPH fluid, coupled by the drag force described in Equation 1.26 (Laibe and Price, 2012):

$$\hat{\rho_{\mathrm{g}}}(\frac{\partial \boldsymbol{v}_{\mathrm{g}}}{\partial t} + \boldsymbol{v}_{\mathrm{g}} \cdot \nabla \boldsymbol{v}) = -\theta \nabla P_{\mathrm{g}} + \hat{\rho} \boldsymbol{f} - \boldsymbol{F}^{V}_{\mathrm{drag}} \tag{1.27}$$

$$\hat{\rho_{\mathrm{d}}}(\frac{\partial \boldsymbol{v}_{\mathrm{d}}}{\partial t} + \boldsymbol{v}_{\mathrm{d}} \cdot \nabla \boldsymbol{v}) = -\nabla P_{\mathrm{d}} - (1 - \theta) \nabla P_{\mathrm{g}} + \hat{\rho} \boldsymbol{f} - \boldsymbol{F}^{V}_{\mathrm{drag}} \tag{1.28}$$

With specific internal energy given by:

$$\frac{\partial u}{\partial t} + (\boldsymbol{v}_{\mathrm{g}} \cdot \nabla) u = -\frac{P_{\mathrm{g}}}{\rho_{\mathrm{g}}} (\nabla \cdot \boldsymbol{v}_{\mathrm{g}}) + K (\boldsymbol{v}_{\mathrm{d}} - \boldsymbol{v}_{\mathrm{g}})^2 \tag{1.29}$$

And stopping time is expressed as (Laibe and Price, 2014a):

$$t_{\mathrm{s}} \equiv \frac{\rho_{\mathrm{d}} \rho_{\mathrm{g}}}{\frac{\hat{\rho_{\mathrm{d}}}}{m_{\mathrm{d}}} K_{\mathrm{s}} (\rho_{\mathrm{g}} + \rho_{\mathrm{d}})}. \tag{1.30}$$

Large stopping times correspond to a weak drag regime and slow dissipation/exchange of energy. Small stopping times correspond to a strong drag regime and disc evolution highly sensitive to momentum or energy exchanges.

The One Fluid Approximation

For computational simplicity, it is possible to re-express all of the two-fluid formalism as a single fluid moving with respect to the center of mass (Laibe and Price, 2014c). This is an incredibly useful approximation in my regime of interest, but is not always valid. We follow Laibe and Price, 2014c for the presentation of equations of motion.

The barycentric velocity is straight forward to find, taking the total density to be $\rho = \rho_{\mathrm{g}} + \rho_{\mathrm{d}}$:

$$\boldsymbol{v} = \frac{\rho_{\mathrm{g}}\boldsymbol{v}_{\mathrm{g}} + \rho_{\mathrm{d}}\boldsymbol{v}_{\mathbf{d}}}{\rho_{\mathrm{g}} + \rho_{\mathrm{d}}}. \tag{1.31}$$

We additionally define the following identities, which allow for the straight forward calculation of the gas and dust velocities respectfully:

$$\boldsymbol{v}_{\mathrm{g}} = \boldsymbol{v} - \frac{\rho_{\mathrm{d}}}{\rho}\Delta\boldsymbol{v} \tag{1.32}$$

$$\boldsymbol{v}_{\mathrm{d}} = \boldsymbol{v} - \frac{\rho_{\mathrm{g}}}{\rho}\Delta\boldsymbol{v} \tag{1.33}$$

Where $\Delta\boldsymbol{v} = \boldsymbol{v}_{\mathbf{g}} - \boldsymbol{v}_{\mathbf{d}}$.

Making substitutions into 1.31, we then simplify using the total time derivative,

$$\frac{d}{dt} = \frac{\partial}{\partial t} + \boldsymbol{v}\cdot\nabla, \tag{1.34}$$

to produce the equations of motion for a Lagrangian frame co-moving with the center of mass of the fluid:

$$\frac{d\rho}{dt} = -\rho(\nabla\cdot\boldsymbol{v}), \tag{1.35}$$

$$\frac{d\boldsymbol{v}}{dt} = \boldsymbol{f} - \frac{\nabla P_{\mathrm{g}}}{\rho} - \frac{1}{\rho}\nabla\cdot\left(\frac{\rho_{\mathrm{g}}\rho_{\mathrm{d}}}{\rho}\Delta\boldsymbol{v}\Delta\boldsymbol{v}\right), \tag{1.36}$$

$$\frac{d}{dt}\left(\frac{\rho_{\mathrm{d}}}{\rho_{\mathrm{g}}}\right) = -\frac{\rho}{\rho_{\mathrm{g}}^2}\nabla\cdot\left(\frac{\rho_{\mathrm{g}}\rho_{\mathrm{d}}}{\rho}\Delta\boldsymbol{v}\right), \tag{1.37}$$

$$\frac{\Delta\boldsymbol{v}}{dt} = -\frac{\Delta\boldsymbol{v}}{t_{\mathrm{s}}} + \frac{\nabla P_{\mathrm{g}}}{\rho_{\mathrm{g}}} - (\Delta\boldsymbol{v}\cdot\nabla)\boldsymbol{v} + \frac{1}{2}\nabla\left(\frac{\rho_{\mathrm{d}} - \rho_{\mathrm{g}}}{\rho_{\mathrm{d}} + \rho_{\mathrm{g}}}\Delta\boldsymbol{v}^2\right), \tag{1.38}$$

And the internal energy given by

$$\frac{du}{dt} = -\frac{P_{\mathrm{g}}}{\rho_{\mathrm{g}}}(\Delta\cdot\boldsymbol{v}_{\mathrm{g}}) + \frac{\rho_{\mathrm{d}}}{\rho}((\Delta\boldsymbol{v}\cdot\nabla)u + \frac{\rho_{\mathrm{d}}}{\rho}\frac{\Delta\boldsymbol{v}^2}{t_{\mathrm{s}}} \tag{1.39}$$

All of the above velocity fields, momenta, densities, and even the energy have singularities at $\rho_{\mathrm{g}} = 0$. This means that portions of the disc that are all dust or very gas depleted diverge numerically, quickly approaching infinity. We are exploring the gaps formed in PPDs, which can have local dearths of gas (Andrews et al., 2018), so this singularity is a problem for my simulation work. Fortunately, it is possible to work around this.

Using the dust fraction, $\epsilon \equiv \rho_{\rm d}\rho^{-1}$, we introduce a parameter we can later use to explicitly and directly evaluate quantities of interest, as well as eliminate our singularity. With a single variable transformation we turn equations 1.35 through 1.39 into the following equations of motion and energy, without any loss of generality (Laibe and Price, 2014c):

$$\frac{d\rho}{dt} = -\rho(\nabla\cdot\boldsymbol{v}), \tag{1.40}$$

$$\frac{d\boldsymbol{v}}{dt} = -\frac{\nabla P_{\rm g}}{\rho} - \frac{1}{\rho}\nabla\cdot(\epsilon(1-\epsilon)\rho\Delta\boldsymbol{v}\Delta\boldsymbol{v}) + \boldsymbol{f}, \tag{1.41}$$

$$\frac{d\epsilon}{dt} = -\frac{1}{\rho}\nabla(\epsilon(1-\epsilon)\rho\Delta\boldsymbol{v}), \tag{1.42}$$

$$\frac{d\Delta\boldsymbol{v}}{dt} = -\frac{\Delta\boldsymbol{v}}{-t_{\rm s}} + \frac{\nabla P_{\rm g}}{(1-\epsilon)\rho} - (\Delta\boldsymbol{v}\cdot\nabla)\boldsymbol{v} + \frac{1}{2}\nabla((2\epsilon-1)\Delta\boldsymbol{v}^2), \tag{1.43}$$

$$\frac{du}{dt} = -\frac{P_{\rm g}}{(1-\epsilon)\rho}\nabla\cdot(\boldsymbol{v}-\epsilon\Delta\boldsymbol{v}) + \epsilon(\Delta\boldsymbol{v}\cdot\nabla)u + \epsilon\frac{\Delta\boldsymbol{v}^2}{t_{\rm s}}, \tag{1.44}$$

And the stopping time is now given by

$$t_{\rm s} = \frac{\epsilon(1-\epsilon)\rho}{K_{\rm s}}. \tag{1.45}$$

Restructuring this problem as one fluid has several advantages computationally, but what cannot be understated is the explicit evolution of the dust-to-gas ratio,ϵ and it's use in constraining both physics and morphology. In Chapter 2 we will be explicitly leveraging ϵ as the basis for my results.

1.2.2 PHANTOM

`PHANTOM` is the SPH code of choice (Price et al., 2018a). It is modular, low-memory, high-performance, and publicly available on the web. For the remainder of the section we present relevant equations and derivations of the smoothing kernal, hydrodynamics, equations of state, timestepping constraints, and artificial viscosity following Price et al., 2018a.

Finding the Smoothing Length and Kernel

The usual SPH conservation of mass, Equation 1.21, prescription helps us to directly place limits on the smoothing kernel, $W(r, h)$:

$$\rho_a = \sum_{\mathrm{b}} m_{\mathrm{b}} W(|\boldsymbol{r}_a - \boldsymbol{r}_{\mathrm{b}}|, h_a) \tag{1.46}$$

where ρ_a is the local density around particle a, m_{b} is the mass of the *b*th particle, and h_a is a smoothing length centered on the a^{th} particle. Importantly, this is a departure from 1.21 by enforcing a particle cut-off such that only a desired number of nearest neighbors[3] is accounted for. The smoothing length must then necessarily scale with local density. `PHANTOM` calculates the smoothing length for particle a as

$$h_a = h_{\mathrm{fact}} n_a^{-1/3} = h_{\mathrm{fact}} (\frac{m_a}{\rho_a})^{1/3} \tag{1.47}$$

ρ and h being mutually dependent introduces another wrinkle: Equations 1.46 and 1.47 must be solved simultaneously. If we rearrange 1.47, it is possible to express ρ_a as a function of h_a:

$$\rho_a(h_a) = m_a(h_{\mathrm{fact}}/h_a)^3 \tag{1.48}$$

We then directly compare this expression for ρ_a to 1.46, and claim convergence for a solution to the smoothing length when $f(h_a) = 0$, where:

$$f(h_a) = \rho_{\mathrm{sum}}(h_a) - \rho_a(h_a) \tag{1.49}$$

After an initial guess, this can be solved to a desired tolerance, iterating with the Newton-Raphson method:

$$h_{\mathrm{a,new}} = h_a - \frac{f(h_a)}{f'(h_a)} \tag{1.50}$$

With a smoothing length chosen, the last step in unraveling mass conservation is the explicit choice of the smoothing kernel. Begin by defining the kernel function thusly:

$$W_{\mathrm{ab}}(r, h) \equiv \frac{C_{\mathrm{norm}}}{h^3} f(q) \tag{1.51}$$

[3] For my use, the average number of nearest neighbors is 57.9 (Price et al., 2018a).

With C_{norm} being set both by the choice of $f(q)$ and dimensions. The default function for $f(q)$ in `PHANTOM` is a M_4 cubic spline and has been the SPH standard for 30 years (Monaghan and Lattanzio, 1985):

$$f(q) = \begin{cases} 1 - \frac{3}{2}q^2 + \frac{3}{4}q^3 & 0 \leq q < 1; \\ \frac{1}{4}(2-q)^3 & 1 \leq q < 2; \\ 0 & q \geq 2. \end{cases} \tag{1.52}$$

This choice of spline has a normalization constant of $C_{\mathrm{norm}} = 1\pi^{-1}$. For more discussion regarding specific splines and the benefit therein, Price et al., 2018a has justifications and benchmarks.

Hydrodynamics

The N-S equations for solving compressible hydrodynamics in `PHANTOM` are presented as:

$$\frac{d\boldsymbol{v}}{dt} = -\frac{\nabla P}{\rho} + \Pi_{\mathrm{shock}} + \boldsymbol{a}_{\mathrm{ext}}(\boldsymbol{r}, t) + \boldsymbol{a}_{\mathrm{sink-gas}} \tag{1.53}$$

$$\frac{du}{dt} = -\frac{P}{\rho}(\nabla \cdot \boldsymbol{v}) + \Lambda_{\mathrm{shock}} - \frac{\Lambda_{\mathrm{cool}}}{\rho} \tag{1.54}$$

Where P is pressure, u is specific internal energy, and Π_{shock} and Λ_{shock} describe dissipation at shock fronts. There are two components to acceleration: $\boldsymbol{a}_{\mathrm{ext}}$ for the 'external' force of the planet, and $\boldsymbol{a}_{\mathrm{sink-gas}}$ for the central star. Both are treated as a standard gravitational potentials, $\Phi = -GM \cdot r^{-1}$, and the latter as a `PHANTOM` sink particle. When gas reaches a specified accretion radius with respect to the sink particle, that gas particle is destroyed and it's mass is added to the star.

Equations of State

For an ideal gas, pressure is given by:

$$P = (\gamma - 1)\rho u \tag{1.55}$$

where γ is the adiabatic index and ρ is the density. The sound speed, c_{s}, is:

$$c_{\mathrm{s}} = \sqrt{\frac{\gamma P}{\rho}} \tag{1.56}$$

And $PV = nRT$ can be re-expressed as:

$$P = \frac{\rho k_\mathrm{b} T}{\mu m_\mathrm{H}} \tag{1.57}$$

Substituting into Equation 1.55 and solving for T:

$$T = \frac{\mu m_\mathrm{H}}{k_\mathrm{B}}(\gamma - 1)u \tag{1.58}$$

where k_B is the Boltzmann constant, μ is the mean molecular weight, and m_H is the mass of a hydrogen atom. The default equations of state take $\gamma = \frac{5}{3}$, and this enables inferences of temperature after gas composition is determined.

Timestepping

The time integration algorithm in `PHANTOM` is a straightforward application of 'Velocity Verlet' (Verlet, 1967), part of the larger Leapfrog family. Particles are updated by a time $\Delta t \equiv t^{n+1} - t^{n}$ following a standard prescription:

$$\boldsymbol{v}^{n+\frac{1}{2}} = \boldsymbol{v}^{n} + \frac{1}{2}\Delta t \boldsymbol{a}^{n} \tag{1.59}$$

$$\boldsymbol{r}^{n+1} = \boldsymbol{r}^{n} + \Delta t \boldsymbol{v}^{n+\frac{1}{2}} \tag{1.60}$$

$$\boldsymbol{a}^{n+1} = \boldsymbol{a}(\boldsymbol{r}^{n+1}) \tag{1.61}$$

$$\boldsymbol{v}^{n+1} = \boldsymbol{v}^{n+\frac{1}{2}} + \frac{1}{2}\Delta t \boldsymbol{a}^{n+1} \tag{1.62}$$

This is a powerful, widely used formulation. Importantly, momentum is conserved to machine precision and long-term energy drift is negligible. There is however one wrinkle introduced by SPH: there are velocity dependent terms that appear in the acceleration due to shock. To account for this 1.61 becomes $\boldsymbol{a}^{n+1} = \boldsymbol{a}(\boldsymbol{r}^{n+1}\boldsymbol{v}^{*})$ with $\boldsymbol{v}^{*}$ being an additional intermediary term:

$$\boldsymbol{v}^{*} = \boldsymbol{v}^{n+\frac{1}{2}} + \frac{1}{2}\Delta t \boldsymbol{a}^{n} \tag{1.63}$$

and a final velocity given by:

$$\boldsymbol{v}^{n+1} = \boldsymbol{v}^{*} + \frac{1}{2}\Delta t[\boldsymbol{a}^{n+1} - \boldsymbol{a}^{n}] \tag{1.64}$$

All that remains now is to determine a Δt, which is determined at the end of each step. The timestep chosen must be shorter than the maximum stable timestep for any of the given particles (Lattanzio et al., 1986a; Monaghan, 1997). For the a^{th} particle the maximum stable timestep is given by

$$\Delta t_{\mathrm{C,a}} \equiv C_{\mathrm{cour}} \frac{h_a}{v_{\mathrm{sig,a}}^{\mathrm{dt}}} \tag{1.65}$$

where h_a is the smoothing length for the a^{th} particle, is $C_{\mathrm{cour}} = 0.3$ by default (Lattanzio et al., 1986b), and $v_{\mathrm{sig,a}}^{\mathrm{dt}}$ is the maximum signal speed through the medium.

There are 4 additional constraints (Price et al., 2018a):

A force condition

$$\Delta t_{\mathrm{f,a}} \equiv C_{\mathrm{force}} \sqrt{\frac{h_a}{|\boldsymbol{a}_a|}} \tag{1.66}$$

An external force condition

$$\Delta t_{\mathrm{ext,a}} \equiv C_{\mathrm{force}} \sqrt{\frac{h_a}{|\boldsymbol{a}_{\mathrm{ext,a}}|}} \tag{1.67}$$

Accelerations towards or away from sink particles

$$\Delta t_{\mathrm{sink-gas,a}} \equiv C_{\mathrm{force}} \sqrt{\frac{h_a}{|\boldsymbol{a}_{\mathrm{sink-gas,a}}|}} \tag{1.68}$$

And external forces who's potential's, Φ, tend towards zero as $r \longrightarrow \infty$

$$\Delta t_{\Phi,\mathrm{a}} \equiv C_{\mathrm{force}} \eta_{\phi} \sqrt{\frac{|\Phi_a|}{|\nabla \Phi|_a^2}} \tag{1.69}$$

For all constraints, $C_{\mathrm{force}} = 0.25$ and for 1.69 $\eta_{\Phi} = 0.05$ are the default options in `PHANTOM` (Price et al., 2018b).

Artificial Viscosity

`PHANTOM` has two different options controlling viscosity. We use the option for implementing α-viscosity (Shakura and Sunyaev, 1973). The explicit prescription is:

$$v = \alpha_{\mathrm{SS}} c_{\mathrm{s}} H \tag{1.70}$$

Where H is the scaleheight of the PPD. Viscosity is calculated following Lodato and Clarke, 2011:

$$\alpha_{\text{SS}} = \frac{1}{10}\alpha_{\text{SPH}}\frac{h}{H} \tag{1.71}$$

α_{SS} is an input parameter for the simulation chosen by the user.

1.3 Disc Evolution Under Planetary Interactions

The primary distinction between a generic accretion disc and a PPD is the presence of planets and/or protoplanets (Andrews, 2015). In the early epochs after stellar formation, planets are liable to form in the remaining dust and gas of that solar nebula that has settled in the disc's midplane (Ida and Lin, 2004; Pollack et al., 1996). The presence of probable exoplanets can be deduced through observations (Pinte et al., 2020; Tsukagoshi et al., 2019), but exact mechanisms of their formation are still an active area of study (D'Angelo and Bodenheimer, 2024; D'Angelo et al., 2021; Kretke and Levison, 2014; Morbidelli and Raymond, 2016). For the purposes of my work we assume the presence of an already formed planet and examine the resulting evolution of the host PPDs under the viscous disc model. Numerical investigations of PPDs with embedded planets have explored a host of masses from fractions of a Neptune mass (Duffell and MacFadyen, 2013), to several Jupiter masses (Duffell, 2020; Fung et al., 2014). These embedded masses can open gaps (Dipierro and Laibe, 2017) and induce spiral wakes (Dong () et al., 2015) through torque interactions, and interactions the gas can also drive migration of the planet (Crida, 2007). This results in a rich system of dynamical evolution; action and reaction cascading. The structure of the simulation we are using allows for these complex dynamics, however we are only attempting to characterize the direct effects gravitational torque and the back reaction.

In the presence of a planet, a graviational torque is excited at Lindblad resonances (Goldreich and Tremaine, 1979) in a parcel of gas of the protoplanetary disc according to:

$$\Lambda(r) = \text{sgn}(r - r_p) f \frac{(GM_p)^2}{\Omega_p^2} \frac{1}{|r - r_p|^4} \tag{1.72}$$

Where f is a constant on the order unity, Ω_p is the Keplerian orbital frequency of the planet, G is the gravitation constant, M_p is the mass of the planet, r_p is the radius of the planet, and r is the location the torque is experienced at. The constant f is the only value that is not an analytical property of the disc or planet, and must be determined through observation and inference (Armitage and Natarajan, 2002).

For a given planetary mass and radial location away from it, the torque exited in the gas described by Equation 1.72 is a constant. A fraction of the torque in the gas phase excited by the planet is then communicated to the dust via drag coupling interactions described by Equation 1.16. Sufficiently powerful torques are able to clear the gas from a region of the PPD around the planet by imparting angular momentum into the gas exterior and taking angular momentum from the gas interior. Dust grains follow the gas flow with responsiveness described by the Stokes number (Equation 1.8 and 1.9). The result is a local depletion of surface density that can be seen in gas and well coupled dust grains (Lin and Papaloizou, 1986). Small grains on the scale of mm and cm radiate in the near-infrared (NIR) and tend to be well coupled to the gas phase (Equation 1.8,Birnstiel et al., 2010). When settled at the midplane of a disc, observations in the NIR can be used to trace gas dynamics at the innermost planet forming regions of PPDs (**simbulan2017**; ALMA Partnership et al., 2015).

1.3.1 Gaps and Measuring Depth

Measurements and analytic descriptions of gaps formed by planets have a long lineage spanning Neptune to Jupiter mass planets in 0, 1, and 2 dimensional simulations (see, e.g., Crida et al., 2006; Duffell and MacFadyen, 2013; Fung et al., 2014; Kanagawa, Tanaka, et al., 2015). Simulations reveal that gaps in in PPDs can be successfully parameterized as functions of the dimensionless K', when dust and effects due to dust are not considered (Kanagawa, Tanaka, et al., 2015; Kanagawa, Muto, et al., 2015). K' contains the mass scale, length scale, and disc viscosity information that all contribute to gap formation:

$$K' = \left(\frac{M_{\rm p}}{M_*}\right)^2 \left(\frac{h_{\rm p}}{r_{\rm p}}\right)^{-5} \alpha^{-1}. \tag{1.73}$$

Using this parametrization scheme, it is possible to express the surface density at the bottom of a gap, $\Sigma_{\rm gap}$, as a ratio of the unperturbed surface density, Σ_0, as a function of K' (Y. A. Tanaka et al., 2022):

$$\frac{\Sigma_{\rm gap}}{\Sigma_0} = \frac{1}{1 + 0.04K'}. \tag{1.74}$$

This analytical method for estimating gap depth and describing shape is widely used and accepted, but does not include effects from dust. Since we are specifically interested in the effects of dust, the lineage of gap depth analysis was useful, but not complete. We found early on that even relatively small changes in ϵ alter the dynamics and morphology of a disc when considering the back reaction of dust.

When simulating ϵ over several orders of magnitude, observed gaps vary greatly in depth, even when taken as a fraction of the initial surface density. Identification of a gap is therefore difficult. To allow for consistent and direct comparison we reduce the azimuthally averaged disc profile following the method of Crida and Morbidelli, 2007. Crida and Morbidelli, 2007 identifies cavities induced by a Jovian planet by comparing surface density profiles of discs simulated with a planet to similar discs simulated without a planet. Thus, gaps and their corresponding depth are identified by their difference from the assumed unperturbed profile, Σ_0.

The variation of ϵ across my simulated discs means that discs were challenging to directly compare. The average azimuthally averaged surface density was subject to vary significantly as we changed gas mass to hold dust mass constant (as seen in Table 1.1), or varied both dust and gas mass to keep total disc mass constant (as seen in Table 1.2). To identify a cavity using the method of Crida and Morbidelli, 2007, we assume that for each simulated disc, an unperturbed disc has a settled dust surface density that follows the general form of a decaying exponential, given by:

$$\Sigma_{\mathrm{background}} = \Sigma_{\mathrm{dust}}|_{R=20\mathrm{au}} \cdot R^{-\zeta}. \tag{1.75}$$

We perform a Levenberg-Marquardt (Marquardt, 1963) fitting routine over the parameter ζ, comparing fitting to the entire azimuthally average profile such that the morphology induced by the planet is minimally captured in $\Sigma_{\mathrm{background}}$. $\Sigma_{\mathrm{dust}}|_{R=20\mathrm{au}}$ is a reference surface density at 20 au, and R is the radius in au for fitting to the profile $\Sigma(R)$.

The resulting fitted surface density profile, $\Sigma_{\mathrm{background}}$, is taken to be an unperturbed surface density, modeling the relaxed surface density without a planet. We then subtract that from the simulated dust surface density profile of the scenario being investigated:

$$\Delta\Sigma_{\mathrm{dust}} = \Sigma_{\mathrm{simulated,dust}} - \Sigma_{\mathrm{background,dust}}. \tag{1.76}$$

Negative values of $\Delta\Sigma_{\mathrm{dust}}$ indicate gaps induced by planets, with the magnitude being the gap depth. We take two measurements for each simulated disc: the max gap depth over the whole profile, and the gap depth at the planetary radiuts from the central star. The unit torque due to a planet goes to zero at the location of the planet (i.e. $r = r_{\mathrm{p}}$, Equation 1.72). We believe this is why some of the azimuthally averaged profiles have a soft "w" shape with the central hump of the "w" located at r_p. The torque density goes to zero, and with reduced torque clearing the gap, gravity from the planet begins to dominate.

This feature disappears in simulations with high ϵ, indicating the role of the back reaction of dust in suppressing this feature.

There is some evidence to suggest a similar soft "w" shape in observations of HL Tau, where there may be some dust in gaps and/or in co-rotation with suspected planets (ALMA Partnership et al., 2015). Simulations of HL Tau reveal that key features, such as the placement and depth of gaps and rings, can be reliably replicated with a combination of three planets (Dipierro, Price, et al., 2015b), we focus on the planet simulated at 68.8 au. This correlates with a slight increase in the inter-gap surface density at approximately 70 au (Meru et al., 2018). We present this to demonstrate that for an azimuthally averaged profile the deepest portion of the gap is not necessarily co-located with the planet, and motivate my use of two different simulated measure.

1.3.2 Planetary Migration

It is prudent to briefly discuss planetary migration as certain scenarios are related to gap formation. My work is not specifically interested in planetary migration, but we do see migration as second and third order effects of changing ϵ.

The simplest type of migration is known as Type 0 and is drift due to the drag experienced by dust grains in gas. Typically seen in small planetesimals, it is possible for planets to under go this type of drag migration (Paardekooper and Papaloizou, 2009). The remaining migration regimes are mediated by viscous interaction.

Planets that are not massive enough to clear their local disc of gas and dust experience Type I migration (H. Tanaka et al., 2002; Ward, 1997). This migration is due to torque felt by the protoplanet from co-rotating elements of the PDD, transferring angular momentum from the planet into the co-rotating elements.

Type II migration occurs when a planet or protoplanet is sufficiently massive to clear its orbit through deposition of torque (Equation 1.72). Assuming that the local density of the gap is sufficiently small, Type I migration cannot take place as any co-rotation torque is too weak (Lin and Papaloizou, 1986). In this prescription the planet is "locked" into it's gap and can only migrate as quickly as the drift velocity of the gas (Nelson et al., 2000).

Type III migration is sometimes called "runaway migration" since drift rate will increase exponentially in certain circumstances (F. S. Masset and Papaloizou, 2003). This migration type occurs for intermediate mass planets that are massive enough to partially clear their local surface density, but are experiencing enough co-rotation torque to begin migrating. This leads to exacerbated torque asymmetries, driving the "runaway" (Artymowicz, 2004).

Table 1.1: Table of simulated disc masses for the constant grain size scenarios. Total dust mass is held constant and ϵ determines gas mass.

ϵ	Dust Mass [$\mathrm{M}_\odot$]	Gas Mass [$\mathrm{M}_\odot$]	Total Mass [$\mathrm{M}_\odot$]
0.005	1×10^{-4}	2×10^{-2}	2.010×10^{-2}
0.01	1×10^{-4}	1×10^{-2}	1.010×10^{-2}
0.05	1×10^{-4}	2×10^{-3}	2.10×10^{-3}
0.1	1×10^{-4}	1×10^{-3}	1.10×10^{-3}
0.5	1×10^{-4}	2×10^{-4}	3.0×10^{-4}

While finalizing my manuscript for publication, I was made aware of work from Guilera et al., 2023 which specifically examines the torque and resulting migration in discs of varying ϵ. They focus on low mass planets ($M_\mathrm{p} < 10 M_\mathrm{Earth}$), but are able to sufficiently alter torques by scaling dust mass to send these planets outward. This suggests a significant dust contribution in torques related to Type I migration, and a potential for local ϵ and dust trapping to have a noticeable effect in Type II migration.

1.4 Simulation Parameter Space

We simulate two scenarios, varying ϵ, dust mass, and the treatment of the back reaction within. In both scenarios, we simulate discs with and without back reaction, and with values of ϵ of 0.005, 0.01, 0.05, 0.10, 0.50. Dust and disc mass treatment is specific to each scenario.

The first scenario is a single constant grain size of $a = 0.1$ mm and a constant total dust mass of $1.00 \times 10^{-4}\mathrm{M}_\odot$ so that dust surface densities are readily comparable between discs.. The change in ϵ varies the total disc mass by setting the gas mass. We use this scenario to approximate continuum observations similar to those used to measure dust mass(ALMA Partnership et al., 2015; Andrews et al., 2012). All of the simulated discs in this scenario would appear to be of approximately the same mass if ϵ is assumed to be $\epsilon_\mathrm{ISM} \sim 0.01$, but in fact have very different total disc masses. See Table 1.1 for the full mass breakdown. In this way, we are able to explore how discs that have similar measured dust masses will have morphologies that vary under changing ϵ, with and without the back reaction.

The second scenario is also under the one-fluid approximation, but instead of setting a constant grain size, we enforce a constant Stokes number of $\mathrm{St} = 0.1$ in the dust phase. This is accomplished by directly setting the stopping time of

Table 1.2: Table of simulated disc masses for constant Stokes numbers scenarios. Total disc mass is held constant with ϵ determining the mass budget.

ϵ	Dust Mass [$\mathrm{M}_\odot$]	Gas Mass [$\mathrm{M}_\odot$]	Total Mass [$\mathrm{M}_\odot$]
0.005	4.98×10^{-6}	9.95×10^{-4}	1.00×10^{-2}
0.01	9.90×10^{-6}	9.90×10^{-4}	1.00×10^{-2}
0.05	4.76×10^{-5}	9.52×10^{-4}	1.00×10^{-2}
0.1	9.09×10^{-5}	9.09×10^{-4}	1.00×10^{-2}

dust particles according to Equation 1.9. For this scenario, the total disc mass is kept constant between simulations. The dust and gas mass are therefore set by the choice of ϵ. See Table 2.2 for the full mass breakdown. These simulations are not meant to approximate any observations, but to probe a regime of constant physics. By keeping drag forces constant, we are able to isolate and generalize the effects of the back reaction.

We use 1 million SPH particles in the one-fluid prescription, and simulate the central star and planet embedded as sink particles of $1\mathrm{M}_\odot$ and $2\mathrm{M}_\mathrm{J}$, respectively, with the planet having an initial orbital radius of 60 au. All discs are initialized with an inner radius of 1 au and an outer radius of 120 au. Discs were evolved for $\sim\ 80$ orbits[4] of the planet as measured by `PHANTOM` to allow the co-orbital region to be sufficiently depleted. Surface density and sound speed profiles follow $\Sigma \propto R^{-1}$ and $c_\mathrm{s} \propto R^{-0.25}$, with values at the disc inner edge (Σ_0 and $c_{\mathrm{s},0}$) set by the disc masses described in Tables 1.1 and 1.2. Sound speed across all scenarios is $c_{\mathrm{s},0} = 0.05\mathrm{cm}\cdot\mathrm{s}^{-1}$. Surface density profiles in the scenarios of constant grain size are set by total disc masses, which is itself determined by the ϵ regime being simulated. These scale from $\Sigma_0 = 238.9\mathrm{g}\cdot\mathrm{cm}^{-2}$ at the lowest ϵ (most massive disc), to $\Sigma_0 = 3.5\mathrm{g}\cdot\mathrm{cm}^{-2}$ at the highest ϵ (least massive disc). The median reference surface density for the scenarios of constant Stokes number is $\Sigma_0 \approx 12\mathrm{g}\cdot\mathrm{cm}^{-2}$, given that all simulations in this scenario use the same total disc mass.

The sink radii are set to 0.800 au for the central star and to 0.25 of the Hill radius for the planet. The Hill radius of a planet is the distance r_H from a given planet of mass M_p orbiting at a radius r_p where the planet's local gravity dominates the gravity of the central star Hill, 1878; Souami et al., 2020:

$$r_\mathrm{H} \approx r_\mathrm{p} \left(\frac{M_\mathrm{p}}{3M_\odot} \right)^{1/3} . \tag{1.77}$$

[4] Simulations of discs with $\mathrm{St} = 0.1$ and $\epsilon = 0.50$ were unable to progress past $\sim\ 25$. Timesteps needed to accurately resolve drag forces in this regime became prohibitively small.

A dust particle being within the Hill radius of the planet is not immediately accreted, which is why the accretion/sink radius is taken as 25% of the Hill radius.

The α_{SPH} value is set in each disc such that the Shakura-Sunyaev artificial viscosity parameter $\alpha_{\mathrm{SS}} \approx 0.005$ Shakura and Sunyaev, 1973. This is calculated according to Lodato and Clarke, 2011 for a α_{SS} on the order of 0.005, ultimately varying throughout the PPD. Canonical values of α_{SS} for PPDs range from $\alpha = 10^{-4}$ to $\alpha = 10^{-2}$ Mulders, G. D. and Dominik, C., 2012; Pinte, Dent, Ménard, Hales, Hill, Cortes, and de Gregorio-Monsalvo, 2016; Zhang et al., 2018. For the mediation of shock propagation, $\beta_{\mathrm{SPH}} = 2.00$.

CHAPTER 2

USING DISC MORPHOLOGY TO CONSTRAIN DUST-TO-GAS MASS RATIO

Murray, M. H. and C. Hall. To be submitted to the Monthly Notices of the Royal Astronomical Society

2.1 Abstract

We demonstrate the importance of the dust back reaction when simulating protoplanetary discs and suggest a means by which it can be used to constrain dust to gas mass ratio (ϵ) and disc mass, by extension. When considering the back reaction, variation in ϵ leads to variation in morphology. In simulated discs of constant grain size that include the back reaction, we see that increasing ϵ first grows then suppresses the depth of planet induced gaps seen in dust, with the inflection point. If planetary mass can be deduced through another means, such as kinematics, the observed morphology of a disc will constrain ϵ, and allow for ranking the ϵ of two or more discs that host planets of similar mass. Additionally, we propose an update to the current analytical gap depth prescription that includes effects due to the back reaction and variations in ϵ.

2.2 Introduction

There are now over 5000 confirmed exoplanet detections, revealing huge diversity in the exoplanet architecture. Arguably the most fundamental exoplanet properties are semi-major axis and mass, which vary over four to five orders of magnitude in the known population (Zhu and Dong, 2021). A planet's semi-major axis may be heavily influenced by planet-disc interactions that lead to migration early in the disc's life (Kley and Nelson, 2012), but may also continue to evolve under secular interactions well after disc dispersal (Ida et al., 2000). Obtaining an accurate measurement of protoplanetary disc (PPD) mass is crucial to understanding the diversity of exoplanets, because planetary masses are constrained by the overall mass budget in a PPD.

Disc mass is also one of the most challenging characteristics to constrain through observations. The molecule with the largest share by mass of any PPD, molecular hydrogen, emits very weakly at typical disc temperatures (Carmona, 2010). As a result, total mass estimates are challenging to obtain directly, and are typically inferred indirectly.

One of the most common methods of determining PPD mass involves using a tracer molecule such as CO, which is about 10 million times more emissive than H_2 at typical disc temperatures (Bergin and Williams, 2017). However, this is not without complications. The lines of some CO isotopologues may be optically thick, therefore only tracing the upper layers of the disc and masking emission from deeper layers which gives an incomplete account of the total emission from that tracer. Additionally, there are uncertainties in the assumed abundances which may be affected and altered by chemical reactions and photodissociation. An alternative that has emerged recently is the measurement or constraint of disc mass through dynamical (Lodato et al., 2023; Veronesi et al., 2021, 2024) or kinematic means (Hall et al., 2020; Longarini et al., 2021; Pinte et al., 2023; Terry et al., 2022), although this requires that the disc be sufficiently massive to be self-gravitating.

Historically, one of the most common methods to obtain disc mass has been to use the brightness of the continuum emission to obtain the total dust mass (Andrews et al., 2012), and then infer both the gas and total mass based on an assumed dust-to-gas ratio, ϵ. Measuring the total dust emission is less challenging since it emits over a continuum, but there are still significant sources of uncertainty. For example, the dust opacity can vary widely depending on a number of assumed properties such as temperature, composition, size, and porosity, such that the dust emission can be either optically thin or thick at millimeter wavelengths based on the choice of dust opacity (Xin et al., 2023). Particles of larger sizes (typically $\sim$mm and above) undergo differential settling and radial drift, resulting in size segregation of grains across the disc (Youdin and Lithwick, 2007).

Perhaps the strongest source of uncertainty is the assumed ϵ. Best estimates for ϵ in the interstellar medium (ISM) are $\epsilon \sim 0.01$ (Frisch and Slavin, 2003; Frisch et al., 2011; Nguyen et al., 2018), and as a result this is a commonly assumed value for PPDs. However, this is likely an oversimplification. For example, observations of CO have found that the average disc ϵ values can be substantially higher, reaching around 0.2 (Ansdell et al., 2016). Similarly, simulations, such as those by **Lebreuilly2020**, have shown that discs can form with significant dust enrichment. Compounding this is the large discrepancy between the observed radial extent of the gas and dust disc components, with the latter typically appearing far more compact (Andrews et al., 2012; Pérez et al., 2012, 2015) due to a combination of grain growth and radial drift. In the most extreme cases, such as IM Lup (Cleeves et al., 2016), the dust disc can be 10 times more compact than its gas component, and since $\epsilon = \epsilon_{\rm ISM}[R_{\rm gas\,disc}/R_{\rm dust\,disc}]^2$ (Ilee et al., 2020), this could potentially result in ϵ values as high as $\epsilon = 1.0$ in the inner $\sim$ 120 au of the disc.

Observations with the Atacama Large Millimeter/submillimeter Array (ALMA) over the last decade have identified a plethora of substructure within PPDs, in particular rings and gaps in the dust continuum (ALMA Partnership et al., 2015; Andrews et al., 2018), spirals (Huang et al., 2018), and velocity perturbations in CO line emission (Paneque-Carreño et al., 2021; Pinte et al., 2018; Teague et al., 2018). Localised velocity perturbations are a strong indication of the kinematic influence of protoplanets (Pinte et al., 2020), which may lead to the formation of these observed disc structures.

The formation of gaps have been shown to have width and depth informed by planetary and disc properties (Duffell and MacFadyen, 2013; Kanagawa, Tanaka, et al., 2015; Kanagawa, Muto, et al., 2015; Kanagawa et al., 2016; Y. A. Tanaka et al., 2022). The current prescription considers disc scale height and viscosity, and planetary mass as factors contributing to gap depth. When any three of gap depth, scale height, viscosity, and planetary mass are well constrained, the fourth can be constrained under this analytical prescription. However, the above prescription was developed without considering dust, so it is difficult to constrain ϵ or estimate the effects of dust-gas coupling on gap formation.

In this work, we demonstrate how changing the global ϵ ratio affects the morphology of a PPD with an embedded planet. This could be used to constrain the ϵ values in observed systems, in particular in systems where protoplanet mass is constrained by kinematics or other means. Additionally, we demonstrate that the current analytical prescription for determining the gap depth induced by a planet is incomplete. A more robust prescription should also consider the effects of ϵ, as well as the back-reaction and coupling regime of the dust.

The paper is organised as follows: in Section 2.3, we discuss the initial conditions of the simulations, as well as our choice of parameter space and measurement of simulated morphological properties. In Section 2.4, we describe our results and a short discussion of the scenarios arising from . In Section 2.4.3 we compare the trends we observe in gap depth due to ϵ and including or excluding the effects of the back reaction from the dust to the gas. In Section 2.5 we present conclusions and discuss limitations, as well as future work and potential questions raised by this study.

2.3 Method

We perform three-dimensional hydrodynamical simulations of pressure-supported, viscous, dusty, gaseous PPDs containing a single planet using `PHANTOM`, a smoothed particle hydrodynamics (SPH) code (Price et al., 2018b). We use the one-fluid approximation, simulating dust and gas as a single fluid (Laibe and Price, 2014a, 2014b, 2014d) with enforced dust mass conservation (Ballabio et al., 2018). Depths of simulated planet induced gaps are measured by subtracting a fitted surface density profile, which is assumed to be the relaxed azimuthal surface density of the disc, from the azimuthally averaged surface density profile of each simulation.

2.3.1 Smoothed Particle Hydrodynamics

We investigate two scenarios: The first is dust of a constant grain size ($a = 0.1$ mm), and the second is dust of a constant Stokes number ($\mathrm{St} = 0.1$), which is implemented in `PHANTOM` through the stopping time according to:

$$t_\mathrm{s} = \frac{\mathrm{St}}{\Omega_\mathrm{k}}, \tag{2.1}$$

where Ω_k is the Keplerian angular frequency. St number is a dimensionless parameter that quantifies drag forces and the degree of coupling felt between different fluids or particles suspended in a fluid (Whipple, 1972). Very small St numbers, $\mathrm{St} << 1$, means that the particle is perfectly coupled to the host fluid and follows the flow extremely closely; a leaf floating in a stream would have a very low St number. Very large St numbers, $\mathrm{St} >> 1$. mean that the particle is perfectly uncoupled from the host fluid and is agnostic to the flow; a rock or large piece of timber in the same stream would have a very large St number. The most interesting regime for St numbers is $\mathrm{St} \sim 1$. In this regime there is partial decoupling between the fluid and suspended particles.

In a PPD, the St number of a species of suspended dust grains can be expressed as (Birnstiel et al., 2010):

$$\mathrm{St} = \frac{\pi a \rho_\mathrm{s}}{2\Sigma_\mathrm{g}}. \tag{2.2}$$

Material density, ρ_s, and particle radius, a, are intrinsic properties of the grain species being considered, while Σ_g is a local property of the disc. As a result, the drag forces between particles and gas are subject to change throughout the disc, even when considering the same dust grain. We simulate discs with a globally enforced St number of 0.1 in order to probe a constant regime of coupling between the gas and the dust. We choose St number of 0.1 as this corresponds to grain sizes on the order of $\sim 0.1 - 1.0$ mm, which are probed with ALMA, while also exploring a particularly interesting coupling regime.

In both scenarios, we simulate discs with and without the back reaction of dust onto the gas while varying ϵ. For a given annulus, the relative azimuthal velocity of the gas and the dust imparts a drag torque, $\Lambda_{\mathrm{g}\rightarrow\mathrm{d}}$, from the gas to the dust of the form (Dipierro and Laibe, 2017):

$$\Lambda_{\mathrm{g}\rightarrow\mathrm{d}} = -r\frac{K}{\rho_\mathrm{d}}(v_{\mathrm{d},\theta} - v_{\mathrm{g},\theta}), \tag{2.3}$$

and the back reaction is an opposite torque, with magnitude scaled by ϵ:

$$\Lambda_{\mathrm{d}\to\mathrm{g}} = -\epsilon\Lambda_{\mathrm{g}\to\mathrm{d}}. \tag{2.4}$$

The constant K is the drag coefficient (Laibe and Price, 2012), and is a function of the stopping time, t_{s}, and the dust-to-gas mass ratio, ϵ:

$$K = \frac{\rho_{\mathrm{d}}}{t_{\mathrm{s}} + \epsilon}. \tag{2.5}$$

When considering the back reaction, net torque on a given annulus of the disc decreases linearly with ϵ:

$$\begin{aligned} \Lambda_{\mathrm{net}} &= \Lambda_{\mathrm{g}\to\mathrm{d}} + \Lambda_{\mathrm{d}\to\mathrm{g}} \\ &= \Lambda_{\mathrm{g}\to\mathrm{d}} - \epsilon\Lambda_{\mathrm{g}\to\mathrm{d}} \\ &= \Lambda_{\mathrm{g}\to\mathrm{d}}(1-\epsilon). \end{aligned} \tag{2.6}$$

To explore how this changes the disc morphology, we perform simulations at five different values of ϵ: 0.005, 0.01, 0.05, 0.1 and 0.5. For the constant grain size scenario, we hold total dust mass (M_{dust}) constant at 1×10^{-4} $\mathrm{M}_{\odot}$ and vary M_{gas}. Continuum observations can be used to measure M_{dust} and then make inferences about M_{total} by making an assumption about ϵ. However, ϵ is typically an unknown quantity. By varying M_{gas}, we explore the impact that ϵ has on the morphology seen in continuum observations. This offers a qualitative stepping stone for determining ϵ in observed systems that have similar M_{dust}. Simulation masses are given in Table 2.1. For the constant $\mathrm{St} = 0.1$ scenario, the total disc mass is held constant between simulations to explore similar physical regimes. Simulation parameters are given in Table 2.2.

We use 1 million SPH particles in the one-fluid prescription, and simulate the central star and planet embedded as sink particles of $1\mathrm{M}_{\odot}$ and $2\mathrm{M}_{\mathrm{J}}$ (Bate et al., 1995), respectively, with the planet having an initial orbital radius of 60 au. The sink radii are set to 0.800 au for the central star and to 0.25 of the Hill radius for the planet (Hill, 1878). All discs are initialized with an inner radius of 1 au and an outer radius of 120 au. Discs are evolved either for 80 orbits at the location of the planet or until the timestep required to accurately resolve the drag force became prohibitively small (minimum of 25 orbits for all simulations).

Surface density and sound speed profiles follow $\Sigma \propto R^{-1}$ and $c_{\mathrm{s}} \propto R^{-0.25}$, with values at the disc inner edge (Σ_0 and $c_{\mathrm{s},0}$) set by the disc masses described in Tables 2.1 and 2.2. Sound speed across all scenarios is $c_{\mathrm{s},0} = 0.05\mathrm{cm} \cdot \mathrm{s}^{-1}$. Surface density profiles in the scenarios of constant grain size are set by total

Table 2.1: Table of simulated disc masses for the constant grain size scenarios. Total dust mass is held constant and ϵ determines gas mass.

ϵ	Dust Mass [$M_\odot$]	Gas Mass [$M_\odot$]	Total Mass [$M_\odot$]
0.005	1×10^{-4}	2×10^{-2}	2.010×10^{-2}
0.01	1×10^{-4}	1×10^{-2}	1.010×10^{-2}
0.05	1×10^{-4}	2×10^{-3}	2.10×10^{-3}
0.1	1×10^{-4}	1×10^{-3}	1.10×10^{-3}
0.5	1×10^{-4}	2×10^{-4}	3.0×10^{-4}

Table 2.2: Table of simulated disc masses for constant St numbers scenarios. Total disc mass is held constant with ϵ determining the mass budget.

ϵ	Dust Mass [$M_\odot$]	Gas Mass [$M_\odot$]	Total Mass [$M_\odot$]
0.005	4.98×10^{-6}	9.95×10^{-4}	1.00×10^{-2}
0.01	9.90×10^{-6}	9.90×10^{-4}	1.00×10^{-2}
0.05	4.76×10^{-5}	9.52×10^{-4}	1.00×10^{-2}
0.1	9.09×10^{-5}	9.09×10^{-4}	1.00×10^{-2}

disc masses, which is itself determined by the ϵ regime being simulated. These scale from $\Sigma_0 = 238.9\text{g} \cdot \text{cm}^{-2}$ at the lowest ϵ (most massive disc), to $\Sigma_0 = 3.5\text{g} \cdot \text{cm}^{-2}$ at the highest ϵ (least massive disc). The median reference surface density for the scenarios of constant St number is $\Sigma_0 \approx 12\text{g} \cdot \text{cm}^{-2}$, given that all simulations in this scenario use the same total disc mass.

The α_{SPH} value is set in each disc such that the Shakura-Sunyaev artificial viscosity parameter $\alpha_{\text{SS}} \approx 0.005$ (Shakura and Sunyaev, 1973), within the accepted range of canonical values of α_{SS} for PPDs ($\alpha = 10^{-4}$ to $\alpha = 10^{-2}$; Mulders, G. D. and Dominik, C., 2012; Pinte, Dent, Ménard, Hales, Hill, Cortes, and de Gregorio-Monsalvo, 2016; Zhang et al., 2018). For all discs, $\beta_{\text{SPH}} = 2.00$.

2.3.2 Measurement of Planet Induced Gap Depth

The shape and depth of gaps induced by planetary interactions are jointly functions of planet and disc properties with a long lineage of analytic descriptions spanning Neptune to Jupiter mass planets in 0, 1, and 2 dimensional simulations (see, e.g., Crida et al., 2006; Duffell and MacFadyen, 2013; Fung et al., 2014; Kanagawa, Tanaka, et al., 2015). In this work we follow Y. A. Tanaka et al., 2022, where the minimum surface density (deepest gap) is given by:

$$\frac{\Sigma_{\rm gap}}{\Sigma_0} = \frac{1}{1 + 0.04K'}. \tag{2.7}$$

Here K' is defined as

$$K' = \left(\frac{M_{\rm p}}{M_*}\right)^2 \left(\frac{h_{\rm p}}{r_{\rm p}}\right)^{-5} \alpha^{-1}, \tag{2.8}$$

where $h_{\rm p} \cdot r_{\rm p}^{-1}$ is the disc aspect ratio $c_{\rm s} \cdot (r\Omega_{\rm K})^{-1}$ at the location of the planet.

This analytical method for estimating gap depth and describing shape is widely used and accepted, but does not include effects from dust. We explore the effects of dust on gap morphology by explicitly considering the back reaction, and comparing to our gap depths measured from simulations to the analytical prescription in Equation (2.7). Under our prescription, even relatively low abundances of dust may alter the dynamics and morphology of the disc.

When simulating ϵ over several orders of magnitude, observed gaps vary greatly in depth, even when taken as a fraction of the initial surface density. Identification of a gap is therefore difficult. To allow for consistent and direct comparison we reduce the azimuthally averaged disc profile following the method of Crida and Morbidelli, 2007. In summary, a logarithmic surface density is taken to be the background surface density, and is subtracted from the azimuthally averaged surface density profile. A reduced, azimuthally averaged profile smooths out small perturbations. We assume that an unperturbed disc has a settled dust surface density that follows the general form of a decaying exponential, given by:

$$\Sigma_{\rm background} = \Sigma_{\rm dust}|_{R=20{\rm au}} R^{-\zeta} \tag{2.9}$$

nder our considerations, $\Sigma_{\rm background}$ is the fitted surface density profile, R is radius in au, $\Sigma_{\rm dust}|_{R=20{\rm au}}$ is the reference surface density at 20 au, and ζ is the fitting parameter. Once a background surface density profile, $\Sigma_{\rm background}$ is determined, we subtract that from the dust surface density profile of the given scenario:

$$\Delta\Sigma_{\rm dust} = \Sigma_{\rm simulated,dust} - \Sigma_{\rm background,dust}. \tag{2.10}$$

Negative values of $\Delta\Sigma_{\rm dust}$ indicate gaps induced by planets, with the magnitude being the gap depth. We take two measurements for each simulated disc: the max gap depth over the whole profile, and the gap depth at the planetary radius from the central star. The unit torque due to a planet goes to zero at the location of the planet (i.e. $r = r_\mathrm{p}$, Goldreich and Tremaine, 1979). Some of the azimuthally averaged profiles have a soft "w" shape with the central hump of the "w" located at r_p. Observations suggest something similar in observations of HL Tau, where there may be some dust in gaps and/or in co-rotation with suspected planets (HL Tau: ALMA Partnership et al., 2015; Location of 68.8 au planet: Dipierro, Price, et al., 2015b; Ring location in gaps carved by planets, notable ring at approximately 70 au: Meru et al., 2018). This means that for the azimuthally averaged profile, the deepest portion of the gap is not necessarily co-located with the planet.

2.4 Results

The importance the back reaction when simulating discs is demonstrated in Figure 2.1 and continuing in Figure 2.2. In both figures, the left column are simulations that include the back reaction, and the right column are simulations that do not include the back reaction. In both columns, ϵ increases from top to bottom and from Figure 2.1 to Figure 2.2. At every simulated value of ϵ, dust distribution is remarkably different with and without the back reaction. Simulations with the back reaction have much more even distribution than those without the back reaction. Both sets of simulations have local spots of relatively high dust density, but compared to simulations without the back reaction, simulations that include the back reaction tend to have more dust dispersal and higher average surface density across the entire visualized range.

In Figure 2.1 to Figure 2.2 we also see the back reaction enhancing pressure trapping of grains around the co-orbital region of the planet at low ϵ. At high ϵ the back reaction contributes to gap infilling, potentially hindering gap clearing in the first place. Without the back reaction, dust readily moves towards the central star and pressure trapping around the gap is minimized. Still there is a prominent gap in the co-orbital region of the planet, and it deepens steadily compared to the background behavior of the disc as ϵ increases. Planets are not fixed and are allowed to migrate, and in fact in one scenario we see migration that appears to be a function of ϵ (top left of Figure 2.3).

2.4.1 Depth vs ϵ

Constant Grain Size

Our primary results are shown in Figure 2.3, which shows the gap depths measured from simulations for our two scenarios (constant grain size of $a = 0.1$

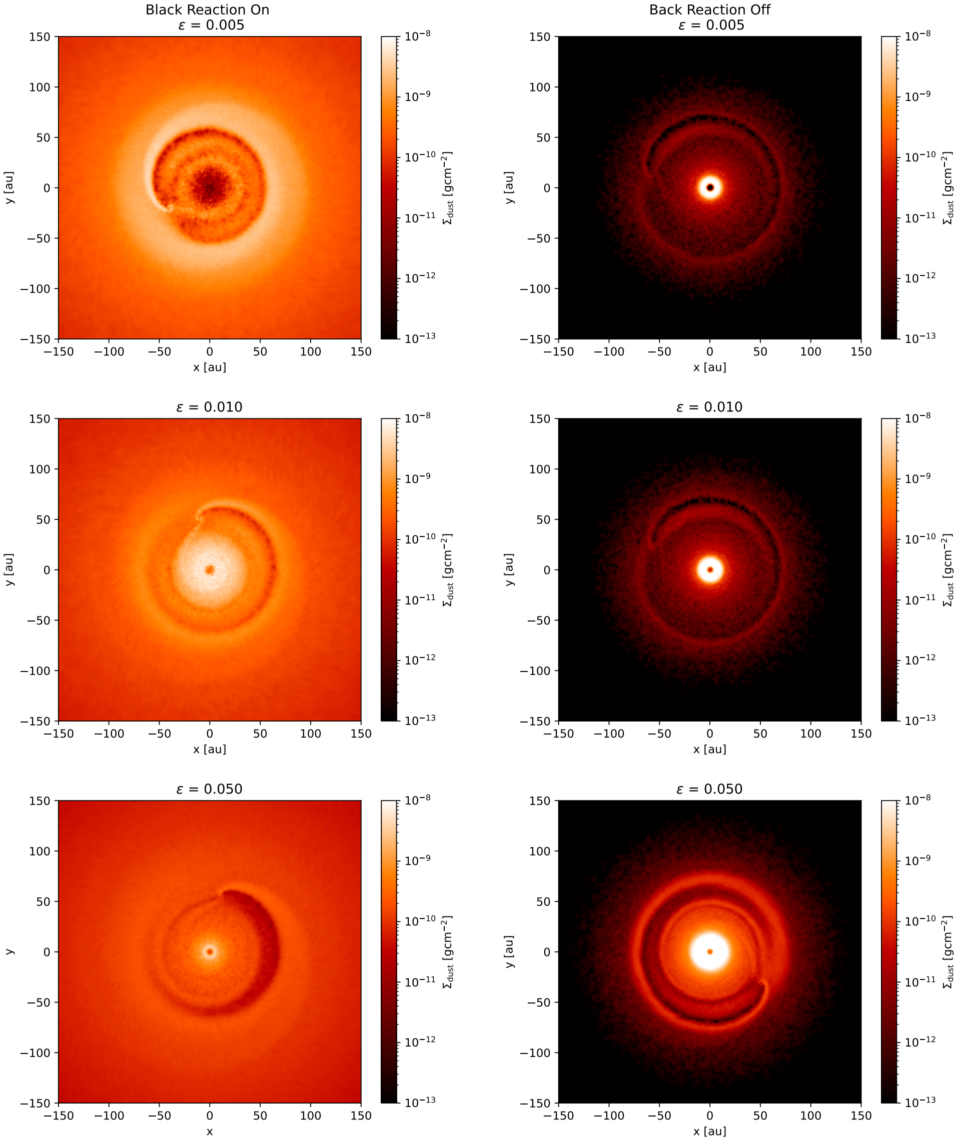

Figure 2.1: Dust surface density of simulated discs with $a = 0.1$mm. The left column is simulated with the back reaction, and the right column is simulated without the back reaction. Each row is a different ϵ, increasing down the page and into Figure 2.2. At every simulated value of ϵ, we see a remarkably different dust distribution. Discs without the back reaction have well defined outer edges at ∼100 au, and larger, higher density inner discs. Discs with the back reaction see a much more even dust dispersal across the visualized range out to 150 au. Additionally there is significant dust trapping near exterior to the orbit of the planet for $\epsilon = 0.005$, indicating at the role the back reaction plays in dust crossing a gap formed by a planet.

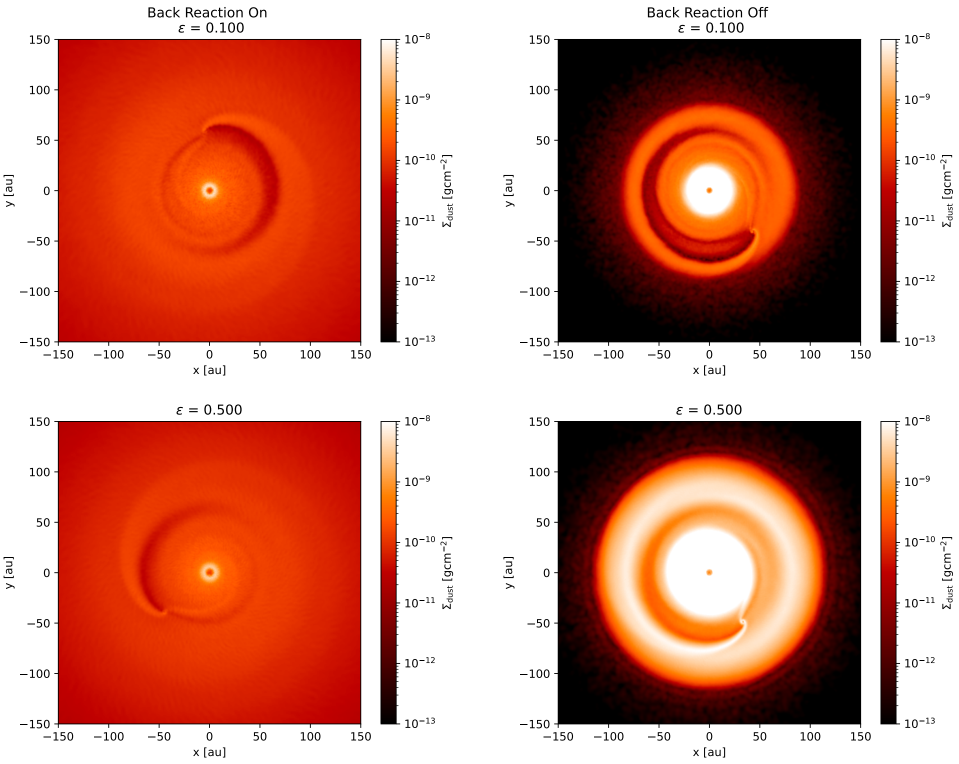

Figure 2.2: Dust surface density of simulated discs with $a = 0.1$mm. The left column is simulated with the back reaction, and the right column is simulated without the back reaction. The top row is $\epsilon = 0.10$ and the bottom row is $\epsilon = 0.50$. The disc that includes the back reaction and with $\epsilon = 0.50$ has the least prominent gap of any of the discs simulated and also has smoothest overall distribution. Additionally, in these high ϵ simulation, the role of ϵ and the back reaction in gap closing is readily apparent. Simulations with the back reaction have gaps spanning a smaller azimuthal angle over all

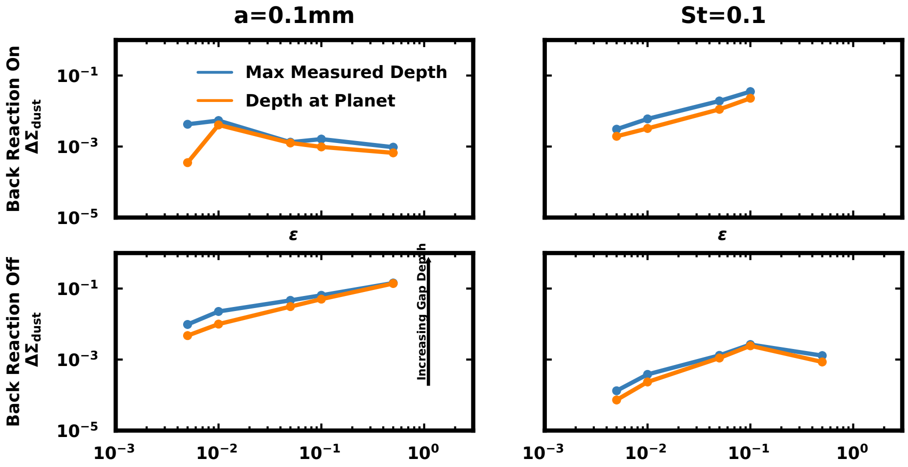

Figure 2.3: Gap depth measured from simulations at the planet location and gap maximum for all simulations. The top row is $\Delta\Sigma_{\text{dust}}$ with the back reaction on and the bottom row is $\Delta\Sigma_{\text{dust}}$ with the back reaction off. The left column shows results for constant grain size of a = 0.1mm, and the right column shows results for constant St number of 0.1. Data sets for St=0.1 with the back reaction is missing a point at $\epsilon = 0.50$. See Note 1.

mm and constant $\mathrm{St} = 0.1$), for the back reaction on and off. This shows simulated gap depth as a function of ϵ, with depth measured at the location of the planet, and also at the deepest point of the gap for all scenarios. In the $a = 0.1$ mm simulations, when the back reaction is included, increasing ϵ results in an increased gap depth from $\epsilon = 0.005$ to $\epsilon = 0.01$. As ϵ increases beyond this, the gap depth decreases. This suggests that there is a sweet spot for ϵ where maximum gap depth can be achieved. This also seems to indicate a consistent regime from $\epsilon = 0.05$ - 0.50, but that space is very coarsely sampled.

When the back reaction is not included, gap depth increases monotonically with ϵ for the $a = 0.1$ mm scenario. This result is consistent with previous findings (e.g. Dipierro et al., 2018), that despite its computational simplicity, neglecting the back reaction results in systems that do not accurately reflect reality. Gap depth continues to increase with increasing ϵ. The ϵ space is too coarsely sampled to develop an analytical prescription, but without the back reaction we do not see any regime change or similar effects.

Constant Stokes Number

We simulate discs of a constant St number of 0.1 with all other parameters described in Section 2.3.1. The right column of Figure 2.3 presents the two different depths measured from simulations vs ϵ, with and without the back reaction. A constant St number means that particles experience a constant rate of coupling. For the chosen St number of 0.1, dust is well coupled to the gas.

With the back reaction included, we see a trend of gap depth increasing as ϵ increases (top right of Figure 2.3). When the back reaction is not included, we see a similar trend of gap depths increasing until $\epsilon = 0.10$, where there is a decrease in gap depths at $\epsilon = 0.50$ (bottom right Figure 2.3). This indicates a potential regime change from "increasing ϵ increases gap depth" to "increasing ϵ decreases gap depth" in the range $\epsilon = 0.10 - 0.50$. Due to $St = 0.1$ with $\epsilon = 0.50$ being computationally prohibitive when the back reaction is included, we do not know if this is due to the lack of the back reaction specifically or changing ϵ in general.

2.4.2 Reduced Profiles

Constant Grain Size

We present the reduced surface density profiles used for the "Depth vs. ϵ" plots in Section 2.4.1 (top left of Figure 2.4). Notable here is the exterior/interior pressure trapping (Dipierro, Pinilla, et al., 2015) of dust at $\epsilon = 0.005$ and $\epsilon = 0.010$ respectively. Additionally the depth regime transition after $\epsilon = 0.010$

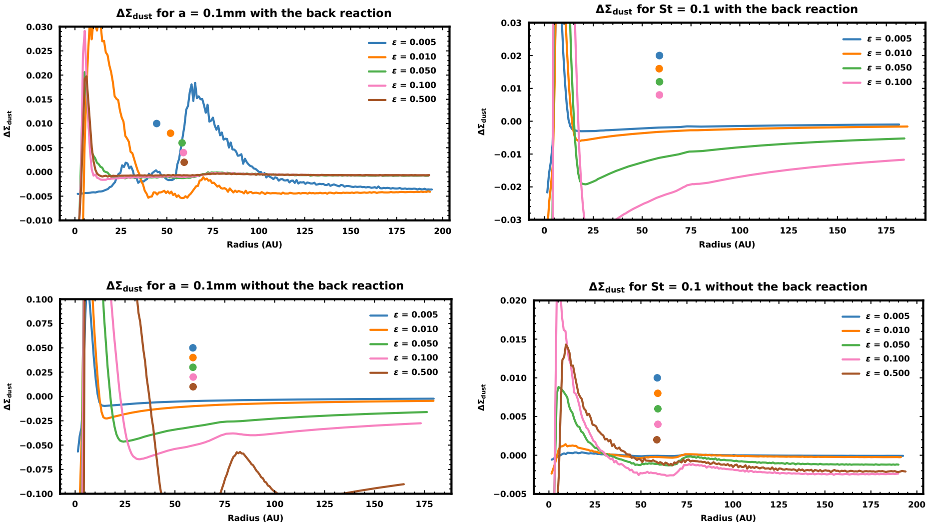

Figure 2.4: Reduced surface densities of simulations with constant grain size of $a = 0.1$ mm (left column) and constant St number of 0.1 (right column). The location of each planet is plotted at it's radius in the same color as the associated profile. Vertical displacement is solely to prevent overplotting in the case of planets being at approximately the same radius. In the bottom left plot, some behavior of the $\epsilon = 0.50$ profile is omitted to better visualize more shallow gap profiles.

is easily identified. At low ϵ we also see the soft "w" shape initially described in Section 2.3.2, indicating there is some dust co-orbiting with the planet. The lowest ϵ has the most co-orbital dust suggesting the back reaction is weakly felt over the span of the gap.

In the case with the back reaction gap width is roughly constant over a particular regime (top left of Figure 2.4), and in the case without the back reaction, the width of the gap varies greatly (bottom left of Figure 2.4). For $\epsilon = 0.005$ and $\epsilon = 0.010$ the gap width is approximately constant when measured against the location of the planet, but gap width appears to have changed due to the planet in these scenarios having migrated by about 10 au. Incidentally, it is also in these simulations that we see the soft "w" initially described in Section 2.3.2. This shape appears in the profile as pronounced inner and outer edges relative to the gap depth, and a small increase of surface density co-located with the planet that appears as a small bump. The middle of the soft "w" and the right/exterior edge of the gap both shift inward by approximately 10 au, seeming to follow the migration of the planet. In the high ϵ regime, post regime transition, gaps have a nearly identical width and almost entirely lose that soft "w", being able to be differentiated only by slight changes in depth. This behavior is different from the bottom left of Figure 2.4, constant grain size without the back reaction, where surface density in the gap decreases dramatically with increasing ϵ.

Constant Stokes Number

For the chosen St number of 0.1, motion is dominated by the gas phase with dust responding according to drag forces. By direct comparison between the reduced surface densities with and without the back reaction, we notice a "smoothing" effect of the back reaction that seems to be accentuated by keeping drag forces constant. Compared to simulations without the back reaction, the profiles in the top right plot of Figure 2.4 lack noise in the surface density and are qualitatively smooth. In the bottom right of Figure 2.4 we see that the simulated profiles have much more noise in the surface density. Additionally, in simulations without the back reaction, there is a soft "w" at high ϵ, most clearly observable in $\epsilon = 0.10$ but also marginally visible in $\epsilon = 0.50$. This indicates the importance of the back reaction in suppressing the "w" feature at high ϵ.

When considering gap depth, it is interesting to note that trends with and without the back reaction are inverse for the two scenarios. For constant grain sizes, gap depth increases monotonically with ϵ when the back reaction is absent. The inverse is true for constant St number, as gap depths increase monotonically with ϵ when the back reaction is present.

2.4.3 The Effect of the Back Reaction on Gap Depth

We demonstrate that including the back reaction distinctly alters the disc morphology from extant prescriptions (Figure 2.5). For the constant grain size scenario (top left of Figure 2.5), including the back reaction results in dust gap depth decreasing with ϵ. If we turn off the back reaction (bottom left of Figure 2.5), the dust gap depth increases with ϵ. A slightly different discrepancy is seen in the constant $\mathrm{St} = 0.1$ scenario. When the back reaction is simulated (top right of Figure 2.5), simulated gap depths are more shallow than the analytical prescription, starting at $\Delta\Sigma_{\mathrm{dust}} \approx 2 \cdot 10^{-3}$, before rising above the analytical prescription to $\Delta\Sigma_{\mathrm{dust}} \approx 4 \cdot 10^{-2}$. The analytical prescription maintains a roughly constant $\Delta\Sigma_{\mathrm{dust}} \approx 1 \cdot 10^{-2}$. When the back reaction is off (bottom right of Figure 2.5), the analytical prescription remains roughly constant on the order of 10^{-2} while simulated depths are one to two orders of magnitude below that for all values of ϵ. This demonstrates that inclusion of the back reaction, even when simulating PPDs with small values of ϵ where the gas torque is (see for example Guilera et al., 2023), is necessary to minimize errors.

Additionally, explicit consideration of the back reaction can be used to constrain ϵ from observations of gap morphology. As it stands our analysis of depths can be used to create a system of relative ranking of ϵ by examining gap depth relative to an unperturbed disc. Unfortunately analysis of gap depths depends on many factors including planetary mass and ϵ, so discs with planets of well known or well constrained mass are needed for this ranking to be effective. That being said, for a number of planets whose masses are similar and constrained through kinematics, one could rank the ϵ_i of each of the host discs through observations of the gaps induced by planetary action, e.g.: $\epsilon_B \leq \epsilon_C << \epsilon_A$, for some selection of discs found to be hosting planets of comparable mass. In conjunction with continuum observations, this also makes disc mass directly comparable.

We have demonstrated that for constant planetary mass, gap depth is dependent on ϵ and the back reaction. If only a few of the discs have masses that are well constrained from other means, it may be possible to straightforwardly derive a "mass ladder" from direct comparison of dust continuum flux.

subsectionComparison to an Analytical Depth Criterion

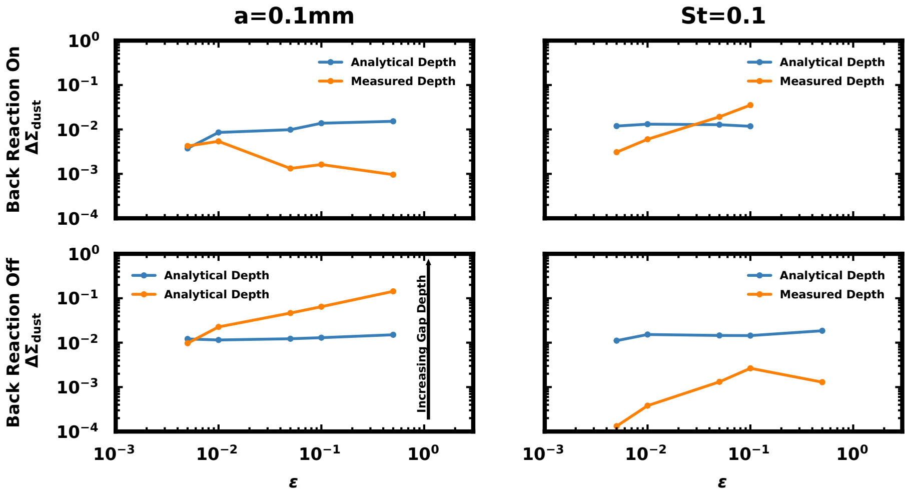

Figure 2.5: Gap depth measured from simulations in dust density compared to the analytical prescription from Y. A. Tanaka et al., 2022 (Equation (2.7)). In the simulations with constant grain size, gaps in dust are suppressed by the back reaction as ϵ increases (top left). Without the back reaction, gaps increase as ϵ increases (bottom left). Neither has good agreement with the analytical prescription. In the simulations with constant St number, there is an apparent regime transition around $\epsilon = 0.10$ without the back reaction (bottom right). Unfortunately, $\epsilon = 0.50$ was computationally prohibitive with the back reaction on, so it is unclear if that regime transition would be present there as well (top left).

We solve for an analytical gap depth estimation provided by Equation (2.7) for each disc. We then make a direct comparison to the gap depth measurement scheme discussed in Section 2.3.2 by shifting Equation (2.7) into $\Delta\Sigma$ space.

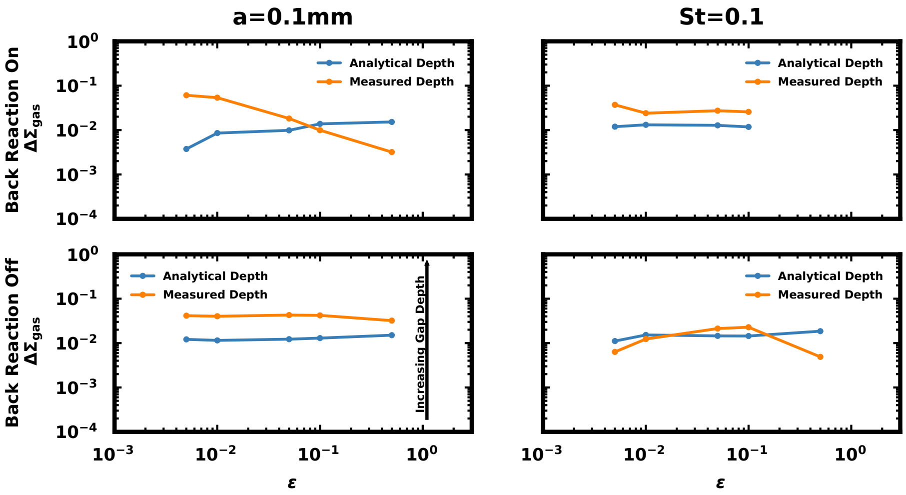

Figure 2.6: Gap depth measured from simulations in gas density compared to the analytical criterion from Y. A. Tanaka et al., 2022 (Equation (2.7)). In the simulations with constant grain size, gaps in gas are suppressed by the back reaction as ϵ increases (top left). In all other scenarios, the gap depth is mostly constant. The only scenario to see numerical agreement with the analytical criterion are the simulations with constant St number and without the back reaction. This scenario is, to a good approximation, the regime under which the criterion was developed: well coupled dust that largely follows the gas, without the back reaction.

This is accomplished by taking

$$\Delta\Sigma = 1 - \frac{\Sigma_{\rm p}}{\Sigma_0}, \qquad (2.11)$$

and assumes that for a surface density profile with no gap, $\Sigma_{\rm NoGap} = \Sigma_0$. We compare this to our simulated gap depths for $\Delta\Sigma_{\rm dust}$ and $\Delta\Sigma_{\rm gas}$ in both scenarios, with and without the back reaction. Results are presented in Figure 2.5 for the dust phase, and Figure 2.6 for the gas phase. The scale heights of each simulation measured at the planetary radius, $h_{\rm p}$, are all relatively constant at ~ 2.6 au, not changing directly as a strong function of ϵ. We note that the analytical gap depth prescription from Y. A. Tanaka et al., 2022 is independent with respect to ϵ, but see a noticeable dependence on ϵ for gap depths measured from simulations. For each scenario, we fit a lograthmic function, ϵ^{ξ} where ξ is a fitting constant, unique and fitted to each scenario. We show that each scenario and has it's own ϵ dependence, where gap depth, $\Delta\Sigma_{\rm dust}$, goes as:

$$\Delta\Sigma_{\rm dust} \propto \epsilon^{\xi}. \qquad (2.12)$$

We present a plot of gap depths measured from simulations, analytical gap depths, and ϵ^{ξ} in Figure 2.7. All scenarios are distinct from each other as functions of ϵ, and no simulation set has the same behavior as the analytical prescription.

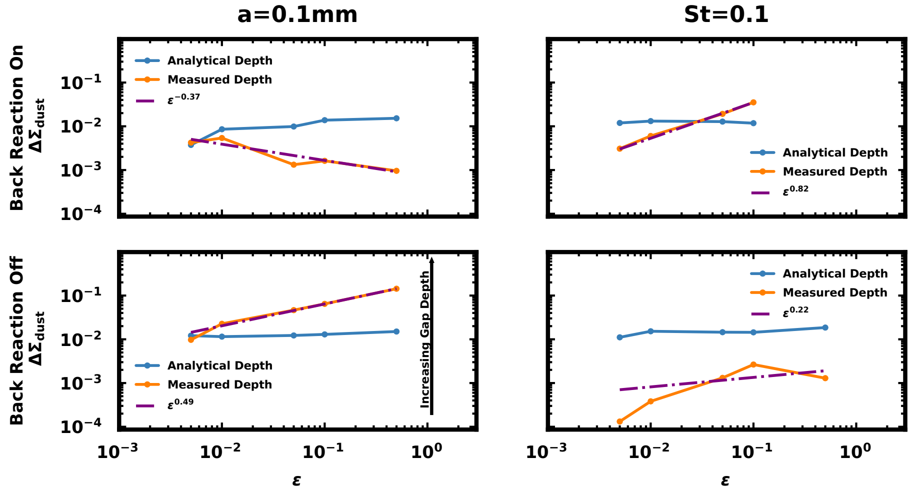

Figure 2.7: Gap depth in dust density measured from simulations compared to the analytical prescription from Y. A. Tanaka et al., 2022 (Equation (2.7)), as well as a plot of ϵ^{ξ}. All simulations and scenarios have behavior that is distinct from the analytical prescription and from each other. Each parameter, ξ, is presented in the legend of the related scenario.

For the scenario of constant grain size, initially considering only the dust, the analytical estimation from Equation (2.7) and our gap depths measured from simulations start with some agreement at $\epsilon = 0.005$ and $\epsilon = 0.01$, but diverge as ϵ increases to 0.10 and beyond. A possible explanation are the length scales of K' changing. The inward migration seen by planets for low values of ϵ may be meaningfully changing the analytically determined gap depth via the factor of r_{p}^{5} in K' (Equation (2.8)). Since h_{p} is roughly constant between simulations, the planetary migration that is only seen for $\epsilon = 0.005$ and $\epsilon = 0.01$ results in length scales that bring our gap depths measured from simulations into agreement with the analytical gap depth. It is unclear if this is incidental or related to the mechanisms that are driving migration in the first place.

In a dusty, viscous, pressure supported PPD, torque excited in the gas by the presence of a planet will be communicated to the dust via drag interactions, with the drag torque from gas onto dust given by Equation (2.3). At the same time, dust exerts a torque back on the gas via mutual drag (Equation (2.4)). This is back reaction and is proportional to the dust-to-mass ratio, ϵ. Comparison to the analytical depth criterion of Y. A. Tanaka et al., 2022 reveals that there is a critical dependence on ϵ that is lacking.

Using continuum observations, it is possible to estimate the surface density, Σ_{dust} of dust (Birnstiel et al., 2018; Landgraf et al., 2000). With some information about scale height or dust settling, it is possible to recover the dust density, ρ_{dust} (Pinte, Dent, Ménard, Hales, Hill, Cortes, and Gregorio-Monsalvo, 2016). With dust density, a measured gap depth can be used to determined a constrained ϵ, since we have shown there is a clear dependence on ϵ in our gap depths measured from simulations.

While not as straightforward as the ranking method described in Section 2.4.3, a related analytical method allows for better estimation of ϵ from observations. Expanding the work of Kanagawa, Tanaka, et al., 2015 and Y. A. Tanaka et al., 2022 into a regime that considers the back reaction due to dust provides another analytical tool to constrain ϵ and PPD masses from observations.

2.5 Conclusion and Future Work

2.5.1 Conclusions

We ran a series of SPH simulations with and without the back reaction of dust and varying ϵ to investigate the effects of dust on disc morphology. We measure gap depths in simulated PPDs by comparing each simulated scenario to a fitted logarithmic surface density taken to be the relaxed scenario without a planet. We find that the effect of the back reaction on gap formation due to planetary action is significant, and conventional prescriptions of gap depth need updating to account for the effects of the back reaction. For constant planetary and stellar masses, Equation (2.7) predicts an increasing gap depth as ϵ increases. This is not what is found in simulations when including the back reaction, except for a short regime between $\epsilon = 0.005$ and $\epsilon = 0.01$. In the scenario of constant grain size that included the back reaction, increasing ϵ beyond $\epsilon = 0.01$ decreases gap depth, suggesting a gap depth maximum and/or regime transition around $\epsilon = 0.1$.

One way to observe this is through the loss of a "w" shaped feature that is present in the low ϵ surface density profiles of Section 2.4.2. At sufficient ϵ, the back reaction is able to clear the local surface density bump that forms at $r = r_{\mathrm{p}}$. As local ϵ increases, the bump is smoothed by the back reaction into the rest of the gap making it more shallow and raising the surface density. A planetary torque is still felt by the gas across the entirety of the gap, and transferred into dust according to Equation (2.3), but at high ϵ the net drag torque is insufficient in clearing dust from the area in space over which it is felt. Net torque decreases linearly with ϵ (Equation (2.6)), and theresults of our simulations imply that gaps clear holistically over the entire region. This means that the distance away from $r_{\rm p}$ over which torque is excited in gas and able to clear dust from near the planet changes marginally due to the back reaction, but the efficiency of that clearing is dramatic. With regards to gap width, the inclusion of the back reaction and changing ϵ has little effect. However, gap depth is sensitive to changing ϵ. As a gap is cleared and ϵ increases locally at the gap edge, the back reaction makes clearing the $(N+1)^{th}$ parcel of dust from the gap more difficult in terms of torque than clearing the N^{th} parcel of dust. In discs with a higher global ϵ, clearing the first parcel of gas requires more torque than the first parcel of gas in a disc with lower global ϵ.

2.5.2 Future Work

We have demonstrated a relationship between ϵ and gap depths that is not fully accommodated by Equation (2.7) and the lineage of Y. A. Tanaka et al., 2022, but more work is required to refine an analytical relationship between ϵ and the gap depth. Our ϵ parameter space was coarsely sampled to demonstrate the overall impact and importance of the effect, but we lack sufficient data to generate a robust model. We suggest that future analysis of the back reaction focus in the regime of $\epsilon \in [0.005, 0.01, 0.05]$ as that is the interval over which the $a = 0.01$ mm scenario transitions from increasing gap depth to decreasing gap depth.

Additionally, holding ϵ constant and varying planetary mass could demonstrate the effect of the back reaction on gap formation through direct comparison to depths estimated from Equation (2.7). This also could be used to provide either a corrective term or an explicit ϵ dependence to the analytical depth formula. Furthermore, we have identified a physically motivated relationship between ϵ, gas density, and the analytical gap depth prescription described by Y. A. Tanaka et al., 2022.

In the presence of planets, we have demonstrated that considering the effects of dust and the back reaction introduces significant variation when ϵ is poorly constrained. Gravitational instability, magnetic effects, and/or streaming instability may similarly respond to changing ϵ and the back reaction in a way that makes constraint or identification more straightforward.

A secondary or tertiary effect beyond the scope of this study is the planetary migration seen in the scenario of constant grain size with the back reaction on. The simulations in which we see the most planetary migration are those with the most mass in gas, and as ϵ increases, total gas mass must necessarily go down to keep dust mass constant. This is consistent with exploration into planetary migration by Quillen et al., 2004 and Crida and Morbidelli, 2007 where it was discussed that planets could not migrate inwards if the planet itself was more massive than the interior gas mass. A recent study from Guilera et al., 2023 provides some additional context to planetary migration under changing ϵ by explicitly considering torque contributions from dust components. They are able to change the sign and magnitude of net torques in the regime of low-mass planets ($M_{\mathrm{p}} \leq 10 M_{\oplus}$) when considering different mass ratios and coupling regimes. We suspect that findings from Guilera et al., 2023 are related to the variation we see in migration, slowing as ϵ increases. Despite our planetary masses not being in the same regime, there is a congruent finding: an increase of ϵ leading to slowed migration. We suspect this is due to an increase in positive torques from dust. Extending the work of Guilera et al., 2023 to $2 M_{\mathrm{Jup}}$ planets will make this hypothesis testable. We suggest a grid-based code; SPH as an algorithm has difficulty with the long timescales typically associated with planetary migration.

2.6 Acknowledgements

Special thanks to Jess Speedie of University of Victoria, British Columbia for insights into observational morphology that resulted in measuring of gap depth relative to the background surface density profile.

Data visualization performed in Figures 2.1 and 2.2 was made possible by the Sarracen Python package (Tricoco, 2023).

This study was supported in part by resources and technical expertise from the Georgia Advanced Computing Resource Center, a partnership between the University of Georgia's Office of the Vice President for Research and Office of the Vice President for Information Technology.

Chapter 3

Conclusion

In this thesis, I present the results from a series of SPH simulations conducted with and without the back reaction while varying ϵ in order to investigate the effects of dust on the morphology of PPDs. By measuring gap depth throughout a variety of scenarios, I have been able to demonstrate the importance of simulating the effects of dust. Increasing ϵ beyond 0.01 was shown to decrease gap depth when simulating the back reaction due to dust and holding grain size constant. This scenario is the most realistic, and through it I demonstrate a general trend of gap depth decreasing as ϵ increases. This trend can be used to constrain values of ϵ in PPDs, and provide more accurate mass measurements for dusty PPDs.

The trend observed in ϵ is, however, degenerate with planetary mass; when ϵ is constant, increasing planetary mass will also increase gap depth. For discs with planets who's masses can be constrained through means other than gap morphology (e.g. velocity perturbation (Terry et al., 2022; Veronesi et al., 2021), it is possible to rank the ϵ of discs with planets of similar masses by measurement of gap depth. Development of an analytical prescription that as robust as Tanaka et al. 2022 requires a much more robust sampling of ϵ-space, but I am able to show that the current prescription needs updating with regards to effects due to dust. The scenario of constant grain size with the back reaction begins with some agreement between simulated and analytical gap depth at low ϵ, but for $\epsilon > 0.01$, analytical gap depths increase while simulated gap depths decrease.

Additionally, the results of our simulations imply that gaps clear holistically over the entire gap width. The distance away from $r_{\rm p}$ over which torque is excited in gas and able to clear dust from near the planet is set by properties of the disc and planet such as relative masses. That distances changes marginally due to the back reaction and with varied ϵ, but the efficiency with which dust is cleared over that region is dramatic. This means that while gap width is not sensitive to the back reaction, gap depth is. This is observed when the back reaction is scaled by changing ϵ.

3.1 Questions Raised and Suggestions for Future Work

In the previous section, I mention that gap depth is degenerate with planetary mass. A parameter space of constant ϵ, ideally for $\epsilon > 0.01$, and varied planetary mass will provide more context to the deficiencies of the current analytical prescription. Importantly, this could help determine if gap depth is actually degenerate with planetary mass or if it only appears to be.

A secondary or tertiary effect that I see due to changing ϵ is variable migration rate of planets in the scenario with constant grain size. While preparing this thesis, there was work indicating a relationship between varied ϵ, dust torques, and migratory behavior of Neptune mass planets (Guilera et al., 2023). Dust torques and migration behaviors were not targets of my investigation, but I believe if this or similar work evaluating dust torques were extended into parameter spaces with more massive planets, it would be possible to discern the underlying mechanism for the migration seen in this work.

BIBLIOGRAPHY

ALMA Partnership, Brogan, C. L., Pérez, L. M., Hunter, T. R., Dent, W. R. F., Hales, A. S., Hills, R. E., Corder, S., Fomalont, E. B., Vlahakis, C., Asaki, Y., Barkats, D., Hirota, A., Hodge, J. A., Impellizzeri, C. M. V., Kneissl, R., Liuzzo, E., Lucas, R., Marcelino, N., … Tatematsu, K. (2015). THE 2014 ALMA LONG BASELINE CAMPAIGN: FIRST RESULTS FROM HIGH ANGULAR RESOLUTION OBSERVATIONS TOWARD THE HL TAU REGION. *The Astrophysical Journal*, *808*(1), L3. https://doi.org/10.1088/2041-8205/808/1/L3

Andrews, S. M. (2015). Observations of Solids in Protoplanetary Disks. *Publications of the Astronomical Society of the Pacific*, *127*(956), 961–993. https://doi.org/10.1086/683178

Andrews, S. M., Huang, J., Pérez, L. M., Isella, A., Dullemond, C. P., Kurtovic, N. T., Guzmán, V. V., Carpenter, J. M., Wilner, D. J., Zhang, S., Zhu, Z., Birnstiel, T., Bai, X.-N., Benisty, M., Hughes, A. M., Öberg, K. I., & Ricci, L. (2018). The Disk Substructures at High Angular Resolution Project (DSHARP). I. Motivation, Sample, Calibration, and Overview. *The Astrophysical Journal*, *869*(2), L41. https://doi.org/10.3847/2041-8213/aaf741

Andrews, S. M., Wilner, D. J., Hughes, A. M., Qi, C., Rosenfeld, K. A., Öberg, K. I., Birnstiel, T., Espaillat, C., Cieza, L. A., Williams, J. P., Lin, S.-Y., & Ho, P. T. P. (2012). The TW Hya Disk at 870 μm: Comparison of CO and Dust Radial Structures., *744*(2), Article 162, 162. https://doi.org/10.1088/0004-637X/744/2/162

Ansdell, M., Williams, J. P., van der Marel, N., Carpenter, J. M., Guidi, G., Hogerheijde, M., Mathews, G. S., Manara, C. F., Miotello, A., Natta, A., Oliveira, I., Tazzari, M., Testi, L., van Dishoeck, E. F., & van Terwisga, S. E. (2016). ALMA Survey of Lupus Protoplanetary Disks. I. Dust and Gas Masses., *828*(1), Article 46, 46. https://doi.org/10.3847/0004-637X/828/1/46

Armitage, P. J., & Natarajan, P. (2002). Accretion during the merger of supermassive black holes. *The Astrophysical Journal*, *567*(1), L9–L12. https://doi.org/10.1086/339770

Artymowicz, P. (2004). Dynamics of Gaseous Disks with Planets [Conference Name: Debris Disks and the Formation of Planets ADS Bibcode: 2004ASPC..324...39A], *324*, 39. Retrieved June 6, 2024, from https://ui.adsabs.harvard.edu/abs/2004ASPC..324...39A

Ballabio, G., Dipierro, G., Veronesi, B., Lodato, G., Hutchison, M., Laibe, G., & Price, D. J. (2018). Enforcing dust mass conservation in 3d simulations of tightly coupled grains with the phantom sph code. *Monthly Notices of the Royal Astronomical Society*, *477*(2), 2766–2771.

Bate, M. R., Bonnell, I. A., & Price, N. M. (1995). Modelling accretion in protobinary systems. *Monthly Notices of the Royal Astronomical Society*, *277*(2), 362–376. https://doi.org/10.1093/mnras/277.2.362

Benítez-Llambay, P., & Masset, F. S. (2016). FARGO3D: A NEW GPU-ORIENTED MHD CODE. *The Astrophysical Journal Supplement Series*, *223*(1), 11. https://doi.org/10.3847/0067-0049/223/1/11

Berger, M., & Colella, P. (1989). Local adaptive mesh refinement for shock hydrodynamics. *Journal of Computational Physics*, *82*(1), 64–84. https://doi.org/10.1016/0021-9991(89)90035-1

Bergin, E. A., & Williams, J. P. (2017). The determination of protoplanetary disk masses. *Formation, Evolution, and Dynamics of Young Solar Systems*, 1–37.

Birnstiel, T., Dullemond, C. P., & Brauer, F. (2010). Gas- and dust evolution in protoplanetary disks., *513*, Article A79, A79. https://doi.org/10.1051/0004-6361/200913731

Birnstiel, T., Dullemond, C. P., Zhu, Z., Andrews, S. M., Bai, X.-N., Wilner, D. J., Carpenter, J. M., Huang, J., Isella, A., Benisty, M., Pérez, L. M., & Zhang, S. (2018). The Disk Substructures at High Angular Resolution Project (DSHARP). V. Interpreting ALMA Maps of Protoplanetary Disks in Terms of a Dust Model. *The Astrophysical Journal Letters*, *869*(2), L45. https://doi.org/10.3847/2041-8213/aaf743

Carmona, A. (2010). Observational Diagnostics of Gas in Protoplanetary Disks. *Earth, Moon, and Planets*, *106*(2-4), 71–95. https://doi.org/10.1007/s11038-009-9347-2

Cleeves, L. I., Öberg, K. I., Wilner, D. J., Huang, J., Loomis, R. A., Andrews, S. M., & Czekala, I. (2016). The Coupled Physical Structure of Gas and Dust in the IM Lup Protoplanetary Disk., *832*(2), Article 110, 110. https://doi.org/10.3847/0004-637X/832/2/110

Crida, A. (2007). Cavity opening by a giant planet in a protoplanetary disc and effects on planetary migration. *Monthly Notices of the Royal Astronomical Society*.

Crida, A., & Morbidelli, A. (2007). Cavity opening by a giant planet in a protoplanetary disc and effects on planetary migration [_eprint: https://academic.oup.com/mnras pdf/377/3/1324/5688238/mnras0377-1324.pdf]. *Monthly Notices of the Royal Astronomical Society*, *377*(3), 1324–1336. https://doi.org/10.1111/j.1365-2966.2007.11704.x

Crida, A., Morbidelli, A., & Masset, F. (2006). On the width and shape of gaps in protoplanetary disks. *Icarus*, *181*(2), 587–604. https://doi.org/10.1016/j.icarus.2005.10.007

D'Angelo, G., & Bodenheimer, P. (2024). Planet Formation by Gas-assisted Accretion of Small Solids. *The Astrophysical Journal*, *967*(2), 124. https://doi.org/10.3847/1538-4357/ad3bae

D'Angelo, G., Weidenschilling, S. J., Lissauer, J. J., & Bodenheimer, P. (2021). Growth of Jupiter: Formation in disks of gas and solids and evolution to the present epoch. *Icarus*, *355*, 114087. https://doi.org/10.1016/j.icarus.2020.114087

Dipierro, G., & Laibe, G. (2017). An opening criterion for dust gaps in protoplanetary discs. *Monthly Notices of the Royal Astronomical Society*, *469*(2), 1932–1948. https://doi.org/10.1093/mnras/stx977

Dipierro, G., Laibe, G., Alexander, R., & Hutchison, M. (2018). Gas and multispecies dust dynamics in viscous protoplanetary discs: The importance of the dust back-reaction. *Monthly Notices of the Royal Astronomical Society*, *479*(3), 4187–4206. https://doi.org/10.1093/mnras/sty1701

Dipierro, G., Pinilla, P., Lodato, G., & Testi, L. (2015). Dust trapping by spiral arms in gravitationally unstable protostellar discs. *Monthly Notices of the Royal Astronomical Society*, *451*(1), 974–986. https://doi.org/10.1093/mnras/stv970

Dipierro, G., Price, D., Laibe, G., Hirsh, K., Cerioli, A., & Lodato, G. (2015a). On planet formation in hl tau. *Monthly Notices of the Royal Astronomical Society: Letters*, *453*(1), L73–L77. https://doi.org/10.1093/mnrasl/slv105

Dipierro, G., Price, D., Laibe, G., Hirsh, K., Cerioli, A., & Lodato, G. (2015b). On planet formation in HL Tau. *Monthly Notices of the Royal Astronomical Society: Letters*, *453*(1), L73–L77. https://doi.org/10.1093/mnrasl/slv105

Dong (), R., Zhu (), Z., Rafikov, R. R., & Stone, J. M. (2015). OBSERVATIONAL SIGNATURES OF PLANETS IN PROTOPLANETARY

DISKS: SPIRAL ARMS OBSERVED IN SCATTERED LIGHT IMAGING CAN BE INDUCED BY PLANETS. *The Astrophysical Journal*, *809*(1), L5. https://doi.org/10.1088/2041-8205/809/1/L5

Duffell, P. C. (2020). An Empirically Derived Formula for the Shape of Planet-induced Gaps in Protoplanetary Disks. *The Astrophysical Journal*, *889*(1), 16. https://doi.org/10.3847/1538-4357/ab5b0f

Duffell, P. C., & MacFadyen, A. I. (2013). Gap Opening by Extremely Low-mass Planets in a Viscous Disk., *769*(1), Article 41, 41. https://doi.org/10.1088/0004-637X/769/1/41

Frisch, P. C., Redfield, S., & Slavin, J. D. (2011). The Interstellar Medium Surrounding the Sun. *Annual Review of Astronomy and Astrophysics*, *49*(1), 237–279. https://doi.org/10.1146/annurev-astro-081710-102613

Frisch, P. C., & Slavin, J. D. (2003). The Chemical Composition and Gas-to-Dust Mass Ratio of Nearby Interstellar Matter. *The Astrophysical Journal*, *594*(2), 844–858. https://doi.org/10.1086/376689

Fung, J., Shi, J.-M., & Chiang, E. (2014). HOW EMPTY ARE DISK GAPS OPENED BY GIANT PLANETS? *The Astrophysical Journal*, *782*(2), 88. https://doi.org/10.1088/0004-637X/782/2/88

Gingold, R. A., & Monaghan, J. J. (1977). Smoothed particle hydrodynamics: Theory and application to non-spherical stars. *Monthly Notices of the Royal Astronomical Society*, *181*(3), 375–389. https://doi.org/10.1093/mnras/181.3.375

Goldreich, P., & Tremaine, S. (1979). The excitation of density waves at the Lindblad and corotation resonances by an external potential., *233*, 857–871. https://doi.org/10.1086/157448

Guilera, O. M., Benitez-Llambay, P., Miller Bertolami, M. M., & Pessah, M. E. (2023). Quantifying the Impact of the Dust Torque on the Migration of Low-mass Planets. *The Astrophysical Journal*, *953*(1), 97. https://doi.org/10.3847/1538-4357/acd2cb

Hall, C., Dong, R., Teague, R., Terry, J., Pinte, C., Paneque-Carreño, T., Veronesi, B., Alexander, R. D., & Lodato, G. (2020). Predicting the Kinematic Evidence of Gravitational Instability., *904*(2), Article 148, 148. https://doi.org/10.3847/1538-4357/abac17

Hammersley, J. M., & Handscomb, D. C. (1964). General Principles of the Monte Carlo Method. In *Monte Carlo Methods* (pp. 50–75). Springer Netherlands. https://doi.org/10.1007/978-94-009-5819-7_5

Harlow, F. H., & Amsden, A. A. (1975). Numerical calculation of multiphase fluid flow. *Journal of Computational Physics*, *17*(1), 19–52. https://doi.org/10.1016/0021-9991(75)90061-3

Hill, G. W. (1878). Researches in the Lunar Theory. *American Journal of Mathematics*, *1*(1), 5. https://doi.org/10.2307/2369430

Hoyle, F. (1960). The Origin of the Solar Nebula [ADS Bibcode: 1960QJRAS...1...28H]. *Quarterly Journal of the Royal Astronomical Society*, *1*, 28. Retrieved June 6, 2024, from https://ui.adsabs.harvard.edu/abs/1960QJRAS...1...28H

Huang, J., Andrews, S. M., Dullemond, C. P., Isella, A., Pérez, L. M., Guzmán, V. V., Öberg, K. I., Zhu, Z., Zhang, S., Bai, X.-N., Benisty, M., Birnstiel, T., Carpenter, J. M., Hughes, A. M., Ricci, L., Weaver, E., & Wilner, D. J. (2018). The Disk Substructures at High Angular Resolution Project (DSHARP). II. Characteristics of Annular Substructures. *The Astrophysical Journal*, *869*(2), L42. https://doi.org/10.3847/2041-8213/aaf740

Ida, S., & Lin, D. N. C. (2004). Toward a Deterministic Model of Planetary Formation. I. A Desert in the Mass and Semimajor Axis Distributions of Extrasolar Planets. *The Astrophysical Journal*, *604*(1), 388–413. https://doi.org/10.1086/381724

Ida, S., Bryden, G., Lin, D. N. C., & Tanaka, H. (2000). Orbital Migration of Neptune and Orbital Distribution of Trans-Neptunian Objects. *The Astrophysical Journal*, *534*(1), 428–445. https://doi.org/10.1086/308720

Ilee, J. D., Hall, C., Walsh, C., Jiménez-Serra, I., Pinte, C., Terry, J., Bourke, T. L., & Hoare, M. (2020). Observing protoplanetary discs with the Square Kilometre Array - I. Characterizing pebble substructure caused by forming planets., *498*(4), 5116–5127. https://doi.org/10.1093/mnras/staa2699

Jacquet, E., Balbus, S., & Latter, H. (2011). On linear dust-gas streaming instabilities in protoplanetary discs: Linear dust-gas streaming instabilities. *Monthly Notices of the Royal Astronomical Society*, *415*(4), 3591–3598. https://doi.org/10.1111/j.1365-2966.2011.18971.x

Jefferys, H. (1924). The cause of cyclones. *Quarterly Journal of the Royal Meteorological Society*, *50*(209), 61–67. https://doi.org/10.1002/qj.49705020914

Kanagawa, K. D., Tanaka, H., Muto, T., Tanigawa, T., & Takeuchi, T. (2015). Formation of a disc gap induced by a planet: Effect of the deviation from Keplerian disc rotation. *Monthly Notices of the Royal Astronomical Society*, *448*(1), 994–1006. https://doi.org/10.1093/mnras/stv025

Kanagawa, K. D., Muto, T., Tanaka, H., Tanigawa, T., Takeuchi, T., Tsukagoshi, T., & Momose, M. (2015). MASS ESTIMATES OF A GIANT PLANET IN A PROTOPLANETARY DISK FROM THE

GAP STRUCTURES. *The Astrophysical Journal*, *806*(1), L15. https://doi.org/10.1088/2041-8205/806/1/L15

Kanagawa, K. D., Muto, T., Tanaka, H., Tanigawa, T., Takeuchi, T., Tsukagoshi, T., & Momose, M. (2016). Mass constraint for a planet in a protoplanetary disk from the gap width [_eprint: https://academic.oup.com/pasj/article-pdf/68/3/43/6847999/psw037.pdf]. *Publications of the Astronomical Society of Japan*, *68*(3). https://doi.org/10.1093/pasj/psw037
43.

Kley, W., & Nelson, R. P. (2012). Planet-disk interaction and orbital evolution. *Annual Review of Astronomy and Astrophysics*, *50*, 211–249. https://doi.org/10.1146/annurev-astro-081811-125523

Kretke, K. A., & Levison, H. F. (2014). CHALLENGES IN FORMING THE SOLAR SYSTEM'S GIANT PLANET CORES VIA PEBBLE ACCRETION. *The Astronomical Journal*, *148*(6), 109. https://doi.org/10.1088/0004-6256/148/6/109

Ladyzhenskaya, O. A. (2003). Sixth problem of the millennium: Navier-Stokes equations, existence and smoothness. *Russian Mathematical Surveys*, *58*(2), 251–286. https://doi.org/10.1070/RM2003v058n02ABEH000610

Laibe, G., & Price, D. (2012). Dusty gas with smoothed particle hydrodynamics - i. algorithm and test suite. *Monthly Notices of the Royal Astronomical Society*, *420*, 2345–2364. https://doi.org/10.1111/j.1365-2966.2011.20202.x

Laibe, G., & Price, D. J. (2012). Dusty gas with smoothed particle hydrodynamics - I. Algorithm and test suite., *420*(3), 2345–2364. https://doi.org/10.1111/j.1365-2966.2011.20202.x

Laibe, G., & Price, D. J. (2014a). Dust and gas mixtures with multiple grain species - a one-fluid approach [arXiv:1407.3569 [astro-ph]]. *Monthly Notices of the Royal Astronomical Society*, *444*(2), 1940–1956. https://doi.org/10.1093/mnras/stu1367
Comment: Accepted for publication in MNRAS.

Laibe, G., & Price, D. J. (2014b). Dusty gas with one fluid [arXiv:1402.5248 [astro-ph]]. *Monthly Notices of the Royal Astronomical Society*, *440*(3), 2136–2146. https://doi.org/10.1093/mnras/stu355
Comment: Accepted for publication in MNRAS (very minor revisions included).

Laibe, G., & Price, D. J. (2014c). Dusty gas with one fluid., *440*(3), 2136–2146. https://doi.org/10.1093/mnras/stu355

Laibe, G., & Price, D. J. (2014d). Dusty gas with one fluid in smoothed particle hydrodynamics [arXiv:1402.5249 [astro-ph]]. *Monthly Notices of the*

Royal Astronomical Society, *440*(3), 2147–2163. https://doi.org/10.1093/mnras/stu359
Comment: Accepted for publication in MNRAS. Numerical code and input files for dustybox, wave and shock tests available from http://users.monash.edu.au/~d

Landgraf, M., Baggaley, W. J., Grün, E., Krüger, H., & Linkert, G. (2000). Aspects of the mass distribution of interstellar dust grains in the solar system from in situ measurements. *Journal of Geophysical Research: Space Physics*, *105*(A5), 10343–10352. https://doi.org/10.1029/1999JA900359

Lattanzio, J. C., Monaghan, J. J., Pongracic, H., & Schwarz, M. P. (1986a). Controlling penetration. *SIAM Journal on Scientific and Statistical Computing*, *7*(2), 591–598. https://doi.org/10.1137/0907039

Lattanzio, J. C., Monaghan, J. J., Pongracic, H., & Schwarz, M. P. (1986b). Controlling Penetration. *SIAM Journal on Scientific and Statistical Computing*, *7*(2), 591–598. https://doi.org/10.1137/0907039

Lebreuilly, U., Commerçon, B., & Laibe, G. (2020). Protostellar collapse: the conditions to form dust-rich protoplanetary disks., *641*, Article A112, A112. https://doi.org/10.1051/0004-6361/202038174

Lin, D. N. C., & Papaloizou, J. (1986). On the Tidal Interaction between Protoplanets and the Protoplanetary Disk. III. Orbital Migration of Protoplanets [Publisher: IOP ADS Bibcode: 1986ApJ...309..846L]. *The Astrophysical Journal*, *309*, 846. https://doi.org/10.1086/164653

Lodato, G., Rampinelli, L., Viscardi, E., Longarini, C., Izquierdo, A., Paneque-Carreño, T., Testi, L., Facchini, S., Miotello, A., Veronesi, B., & Hall, C. (2023). Dynamical mass measurements of two protoplanetary discs., *518*(3), 4481–4493. https://doi.org/10.1093/mnras/stac3223

Lodato, G., & Clarke, C. J. (2011). Resolution requirements for smoothed particle hydrodynamics simulations of self-gravitating accretion discs: Resolving fragmentation in SPH simulations. *Monthly Notices of the Royal Astronomical Society*, *413*(4), 2735–2740. https://doi.org/10.1111/j.1365-2966.2011.18344.x

Longarini, C., Lodato, G., Toci, C., Veronesi, B., Hall, C., Dong, R., & Patrick Terry, J. (2021). Investigating Protoplanetary Disk Cooling through Kinematics: Analytical GI Wiggle., *920*(2), Article L41, L41. https://doi.org/10.3847/2041-8213/ac2df6

Lynden-Bell, D., & Pringle, J. E. (1974). The Evolution of Viscous Discs and the Origin of the Nebular Variables. *Monthly Notices of the Royal Astronomical Society*, *168*(3), 603–637. https://doi.org/10.1093/mnras/168.3.603

Marquardt, D. W. (1963). An Algorithm for Least-Squares Estimation of Nonlinear Parameters [_eprint: https://doi.org/10.1137/0111030]. *Journal* *of the Society for Industrial and Applied Mathematics*, *11*(2), 431–441. https://doi.org/10.1137/0111030

marquis de Laplace, P. S. (1813). *Exposition du système du monde* (Vol. 1). Courcier.

Masset, F. (2000). FARGO: A fast eulerian transport algorithm for differentiallyrotating disks. *Astronomy and Astrophysics Supplement Series*, *141*(1), 165–173. https://doi.org/10.1051/aas:2000116

Masset, F. S., & Papaloizou, J. C. B. (2003). Runaway Migration and the Formation of Hot Jupiters. *The Astrophysical Journal*, *588*(1), 494–508. https://doi.org/10.1086/373892

Meru, F., Rosotti, G. P., Booth, R. A., Nazari, P., & Clarke, C. J. (2018). Is the ring inside or outside the planet?: The effect of planet migration on dust rings [Publisher: arXiv Version Number: 1]. https://doi.org/10.48550/ARXIV.1810.06573
Other 18 pages, 18 figures, accepted for publication in MNRAS.

Monaghan, J. J. (1997). SPH and Riemann Solvers. *Journal of Computational Physics*, *136*(2), 298–307. https://doi.org/10.1006/jcph.1997.5732

Monaghan, J. J., & Lattanzio, J. C. (1985). A refined particle method for astrophysical problems., *149*(1), 135–143.

Morbidelli, A., & Raymond, S. N. (2016). Challenges in planet formation. *Journal of Geophysical Research: Planets*, *121*(10), 1962–1980. https://doi.org/10.1002/2016JE005088

Mulders, G. D. & Dominik, C. (2012). Probing the turbulent mixing strength in protoplanetary disks across the stellar mass range: No significant variations. *AA*, *539*, A9. https://doi.org/10.1051/0004-6361/201118127

Nakagawa, Y., Sekiya, M., & Hayashi, C. (1986). Settling and growth of dust particles in a laminar phase of a low-mass solar nebula. *Icarus*, *67*(3), 375–390. https://doi.org/10.1016/0019-1035(86)90121-1

Nelson, R. P., Papaloizou, J. C. B., Masset, F., & Kley, W. (2000). The migration and growth of protoplanets in protostellar discs. *Monthly Notices of the Royal Astronomical Society*, *318*(1), 18–36. https://doi.org/10.1046/j.1365-8711.2000.03605.x

Nguyen, H., Dawson, J. R., Miville-Deschênes, M.-A., Tang, N., Li, D., Heiles, C., Murray, C. E., Stanimirović, S., Gibson, S. J., McClure-Griffiths, N. M., Troland, T., Bronfman, L., & Finger, R. (2018). Dust–Gas Scaling Relations and OH Abundance in the Galactic ISM. *The Astrophysical Journal*, *862*(1), 49. https://doi.org/10.3847/1538-4357/aac82b

Paardekooper, S.-J., & Papaloizou, J. C. B. (2009). On corotation torques, horseshoe drag and the possibility of sustained stalled or outward protoplanetary migration. *Monthly Notices of the Royal Astronomical Society*, *394*(4), 2283–2296. https://doi.org/10.1111/j.1365-2966.2009.14511.x

Paneque-Carreño, T., Pérez, L. M., Benisty, M., Hall, C., Veronesi, B., Lodato, G., Sierra, A., Carpenter, J. M., Andrews, S. M., Bae, J., Henning, T., Kwon, W., Linz, H., Loinard, L., Pinte, C., Ricci, L., Tazzari, M., Testi, L., & Wilner, D. (2021). Spiral Arms and a Massive Dust Disk with Non-Keplerian Kinematics: Possible Evidence for Gravitational Instability in the Disk of Elias 2-27., *914*(2), Article 88, 88. https://doi.org/10.3847/1538-4357/abf243

Papaloizou, J. C. B., & Lin, D. N. C. (1995). Theory of Accretion Disks I: Angular Momentum Transport Processes. *Annual Review of Astronomy and Astrophysics*, *33*(1), 505–540. https://doi.org/10.1146/annurev.aa.33.090195.002445

Pérez, L. M., Carpenter, J. M., Chandler, C. J., Isella, A., Andrews, S. M., Ricci, L., Calvet, N., Corder, S. A., Deller, A. T., Dullemond, C. P., Greaves, J. S., Harris, R. J., Henning, T., Kwon, W., Lazio, J., Linz, H., Mundy, L. G., Sargent, A. I., Storm, S., … Wilner, D. J. (2012). Constraints on the Radial Variation of Grain Growth in the AS 209 Circumstellar Disk., *760*(1), Article L17, L17. https://doi.org/10.1088/2041-8205/760/1/L17

Pérez, L. M., Chandler, C. J., Isella, A., Carpenter, J. M., Andrews, S. M., Calvet, N., Corder, S. A., Deller, A. T., Dullemond, C. P., Greaves, J. S., Harris, R. J., Henning, T., Kwon, W., Lazio, J., Linz, H., Mundy, L. G., Ricci, L., Sargent, A. I., Storm, S., … Wilner, D. J. (2015). Grain Growth in the Circumstellar Disks of the Young Stars CY Tau and DoAr 25., *813*(1), Article 41, 41. https://doi.org/10.1088/0004-637X/813/1/41

Pinte, C., Dent, W. R. F., Ménard, F., Hales, A., Hill, T., Cortes, P., & de Gregorio-Monsalvo, I. (2016). Dust and Gas in the Disk of HL Tauri: Surface Density, Dust Settling, and Dust-to-gas Ratio., *816*(1), Article 25, 25. https://doi.org/10.3847/0004-637X/816/1/25

Pinte, C., Dent, W. R. F., Ménard, F., Hales, A., Hill, T., Cortes, P., & Gregorio-Monsalvo, I. D. (2016). DUST AND GAS IN THE DISK OF HL TAURI: SURFACE DENSITY, DUST SETTLING, AND DUST-TO-GAS RATIO. *The Astrophysical Journal*, *816*(1), 25. https://doi.org/10.3847/0004-637X/816/1/25

Pinte, C., Price, D. J., Ménard, F., Duchêne, G., Christiaens, V., Andrews, S. M., Huang, J., Hill, T., Van Der Plas, G., Perez, L. M., Isella, A., Boehler, Y., Dent, W. R. F., Mentiplay, D., & Loomis, R. A. (2020). Nine Localized Deviations from Keplerian Rotation in the DSHARP Circumstellar

Disks: Kinematic Evidence for Protoplanets Carving the Gaps. *The Astrophysical Journal*, *890*(1), L9. https://doi.org/10.3847/2041-8213/ab6dda

Pinte, C., Teague, R., Flaherty, K., Hall, C., Facchini, S., & Casassus, S. (2023, July). Kinematic Structures in Planet-Forming Disks. In S. Inutsuka, Y. Aikawa, T. Muto, K. Tomida, & M. Tamura (Eds.), *Protostars and planets vii* (p. 645, Vol. 534). https://doi.org/10.48550/arXiv.2203.09528

Pinte, C., Price, D. J., Menard, F., Duchêne, G., Dent, W. R. F., Hill, T., De Gregorio-Monsalvo, I., Hales, A. S., & Mentiplay, D. (2018). Kinematic evidence for an embedded protoplanet in a circumstellar disc. *The Astrophysical Journal Letters*, *860*(1), L13. https://doi.org/10.3847/2041-8213/aac6dc

Plewa, T., & Müller, E. (2001). AMRA: An Adaptive Mesh Refinement hydrodynamic code for astrophysics. *Computer Physics Communications*, *138*(2), 101–127. https://doi.org/10.1016/S0010-4655(01)00199-0

Pollack, J. B., Hubickyj, O., Bodenheimer, P., Lissauer, J. J., Podolak, M., & Greenzweig, Y. (1996). Formation of the Giant Planets by Concurrent Accretion of Solids and Gas. *Icarus*, *124*(1), 62–85. https://doi.org/10.1006/icar.1996.0190

Price, D. J., Wurster, J., Tricco, T. S., Nixon, C., Toupin, S., Pettitt, A., Chan, C., Mentiplay, D., Laibe, G., Glover, S., Dobbs, C., Nealon, R., Liptai, D., Worpel, H., Bonnerot, C., Dipierro, G., Ballabio, G., Ragusa, E., Federrath, C., … Lodato, G. (2018a). Phantom: A Smoothed Particle Hydrodynamics and Magnetohydrodynamics Code for Astrophysics., *35*, Article e031, e031. https://doi.org/10.1017/pasa.2018.25

Price, D. J., Wurster, J., Tricco, T. S., Nixon, C., Toupin, S., Pettitt, A., Chan, C., Mentiplay, D., Laibe, G., Glover, S., Dobbs, C., Nealon, R., Liptai, D., Worpel, H., Bonnerot, C., Dipierro, G., Ballabio, G., Ragusa, E., Federrath, C., … Lodato, G. (2018b). Phantom: A smoothed particle hydrodynamics and magnetohydrodynamics code for astrophysics [arXiv:1702.03930 [astro-ph]]. *Publications of the Astronomical Society of Australia*, *35*, e031. https://doi.org/10.1017/pasa.2018.25
Comment: 88 pages, 60 figures, accepted to PASA. Code available from https://phantomsph.bitbucket.io/.

Pringle, J. E. (1981). Accretion discs in astrophysics [ADS Bibcode: 1981ARA&A..19..137P]. *Annual Review of Astronomy and Astrophysics*, *19*, 137–162. https://doi.org/10.1146/annurev.aa.19.090181.001033

Quillen, A. C., Blackman, E. G., Frank, A., & Varnière, P. (2004). On the Planet and the Disk of C o K u TAURI/4. *The Astrophysical Journal*, *612*(2), L137–L140. https://doi.org/10.1086/424693

Shakura, N. I., & Sunyaev, R. A. (1973). Black holes in binary systems. Observational appearance., *24*, 337–355.

Souami, D., Cresson, J., Biernacki, C., & Pierret, F. (2020). On the local and global properties of gravitational spheres of influence. *Monthly Notices of the Royal Astronomical Society*, *496*(4), 4287–4297. https://doi.org/10.1093/mnras/staa1520

Speith, R., Riffert, H., & Ruder, H. (1999). Numerical Fluid Dynamics in Astrophysics with Smoothed Particle Hydrodynamics [Series Title: Lecture Notes in Computational Science and Engineering]. In M. Griebel, D. E. Keyes, R. M. Nieminen, D. Roose, T. Schlick, H.-J. Bungartz, F. Durst, & C. Zenger (Eds.), *High Performance Scientific and Engineering Computing* (pp. 417–430, Vol. 8). Springer Berlin Heidelberg. https://doi.org/10.1007/978-3-642-60155-2_35

Stone, H. A. (1994). Dynamics of Drop Deformation and Breakup in Viscous Fluids. *Annual Review of Fluid Mechanics*, *26*(1), 65–102. https://doi.org/10.1146/annurev.fl.26.010194.000433

Tanaka, H., Takeuchi, T., & Ward, W. R. (2002). Three-dimensional Interaction between a Planet and an Isothermal Gaseous Disk. I. Corotation and Lindblad Torques and Planet Migration. *The Astrophysical Journal*, *565*(2), 1257–1274. https://doi.org/10.1086/324713

Tanaka, Y. A., Kanagawa, K. D., Tanaka, H., & Tanigawa, T. (2022). Eccentric Gap Induced by a Super-Jupiter-mass Planet. *The Astrophysical Journal*, *925*(1), 95. https://doi.org/10.3847/1538-4357/ac3af5

Teague, R., Bae, J., Bergin, E. A., Birnstiel, T., & Foreman-Mackey, D. (2018). A Kinematical Detection of Two Embedded Jupiter Mass Planets in HD 163296. *The Astrophysical Journal Letters*, *860*(1), L12. https://doi.org/10.3847/2041-8213/aac6d7

Terry, J. P., Hall, C., Longarini, C., Lodato, G., Toci, C., Veronesi, B., Paneque-Carreño, T., & Pinte, C. (2022). Constraining protoplanetary disc mass using the GI wiggle., *510*(2), 1671–1679. https://doi.org/10.1093/mnras/stab3513

Tricoco, T. (2023). Sarracen: A python package for analysis and visualization of smoothed particle hydrodynamics data. *Journal of Open Source Software, 8(86), 5263*. https://doi.org/10.21105/joss.05263

Tsukagoshi, T., Muto, T., Nomura, H., Kawabe, R., Kanagawa, K. D., Okuzumi, S., Ida, S., Walsh, C., Millar, T. J., Takahashi, S. Z., Hashimoto, J., Uyama, T., & Tamura, M. (2019). Discovery of An au-scale Excess in Millimeter Emission from the Protoplanetary Disk around TW Hya. *The Astrophysical Journal Letters*, *878*(1), L8. https://doi.org/10.3847/2041-8213/ab224c

Verlet, L. (1967). Computer "experiments" on classical fluids. i. thermodynamical properties of lennard-jones molecules. *Phys. Rev.*, *159*, 98–103. https://doi.org/10.1103/PhysRev.159.98

Veronesi, B., Longarini, C., Lodato, G., Laibe, G., Hall, C., Facchini, S., & Testi, L. (2024). Weighing protoplanetary discs with kinematics: physical model, method and benchmark. *arXiv e-prints*, Article arXiv:2405.15944, arXiv:2405.15944. https://doi.org/10.48550/arXiv.2405.15944

Veronesi, B., Paneque-Carreño, T., Lodato, G., Testi, L., Pérez, L. M., Bertin, G., & Hall, C. (2021). A Dynamical Measurement of the Disk Mass in Elias 227., *914*(2), Article L27, L27. https://doi.org/10.3847/2041-8213/abfe6a

von Weizsäcker, C. F. (1948). Zur Kosmogonie. [ADS Bibcode: 1948ZA.....24..181V]. *Zeitschrift fur Astrophysik*, *24*, 181. Retrieved June 6, 2024, from https://ui.adsabs.harvard.edu/abs/1948ZA.....24..181V

Ward, W. R. (1997). Protoplanet Migration by Nebula Tides. *Icarus*, *126*(2), 261–281. https://doi.org/10.1006/icar.1996.5647

Whipple, F. L. (1972). On certain aerodynamic processes for asteroids and comets. *From plasma to planet*, 211.

Xin, Z., Espaillat, C. C., Rilinger, A. M., Ribas, Á., & Macías, E. (2023). Measuring the Dust Masses of Protoplanetary Disks in Lupus with ALMA: Evidence That Disks Can Be Optically Thick at 3 mm. *The Astrophysical Journal*, *942*(1), 4. https://doi.org/10.3847/1538-4357/aca52b

Youdin, A. N., & Goodman, J. (2005). Streaming Instabilities in Protoplanetary Disks. *The Astrophysical Journal*, *620*(1), 459–469. https://doi.org/10.1086/426895

Youdin, A. N., & Lithwick, Y. (2007). Particle stirring in turbulent gas disks: Including orbital oscillations. *Icarus*, *192*(2), 588–604. https://doi.org/10.1016/j.icarus.2007.07.012

Zhang, S., Zhu, Z., Huang, J., Guzmán, V. V., Andrews, S. M., Birnstiel, T., Dullemond, C. P., Carpenter, J. M., Isella, A., Pérez, L. M., Benisty, M., Wilner, D. J., Baruteau, C., Bai, X.-N., & Ricci, L. (2018). The Disk Substructures at High Angular Resolution Project (DSHARP).

VII. The Planet–Disk Interactions Interpretation. *The Astrophysical Journal*, *869*(2), L47. https://doi.org/10.3847/2041-8213/aaf744

Zhu, W., & Dong, S. (2021). Exoplanet Statistics and Theoretical Implications., *59*, 291–336. https://doi.org/10.1146/annurev-astro-112420-020055